

Model-independent determination of the relative strong-phase difference between D^0 and $\bar{D}^0 \rightarrow K_{S,L}^0 \pi^+ \pi^-$ and its impact on the measurement of the CKM angle γ/ϕ_3

M. Ablikim¹, M. N. Achasov^{10,d}, P. Adlarson⁵⁹, S. Ahmed¹⁵, M. Albrecht⁴, M. Alekseyev^{58A,58C}, D. Ambrose⁵¹, A. Amoroso^{58A,58C}, F. F. An¹, Q. An^{55,43}, Anita²¹, Y. Bai⁴², O. Bakina²⁷, R. Baldini Ferroli^{23A}, I. Balossino^{24A}, Y. Ban^{35,l}, K. Begzsuren²⁵, J. V. Bennett⁵, N. Berger²⁶, M. Bertani^{23A}, D. Bettoni^{24A}, F. Bianchi^{58A,58C}, J. Biernat⁵⁹, J. Bloms⁵², I. Boyko²⁷, R. A. Briere⁵, H. Cai⁶⁰, X. Cai^{1,43}, A. Calcaterra^{23A}, G. F. Cao^{1,47}, N. Cao^{1,47}, S. A. Cetin^{46B}, J. Chai^{58C}, J. F. Chang^{1,43}, W. L. Chang^{1,47}, G. Chelkov^{27,b,c}, D. Y. Chen⁶, G. Chen¹, H. S. Chen^{1,47}, J. Chen¹⁶, J. C. Chen¹, M. L. Chen^{1,43}, S. J. Chen³³, Y. B. Chen^{1,43}, W. Cheng^{58C}, G. Cibinetto^{24A}, F. Cossio^{58C}, X. F. Cui³⁴, H. L. Dai^{1,43}, J. P. Dai^{38,h}, X. C. Dai^{1,47}, A. Dbeyssi¹⁵, D. Dedovich²⁷, Z. Y. Deng¹, A. Denig²⁶, I. Denysenko²⁷, M. Destefanis^{58A,58C}, F. De Mori⁵⁹, Y. Ding³¹, C. Dong³⁴, J. Dong^{1,43}, L. Y. Dong^{1,47}, M. Y. Dong^{1,43,47}, Z. L. Dou³³, S. X. Du⁶³, J. Z. Fan⁴⁵, J. Fang^{1,43}, S. S. Fang^{1,47}, Y. Fang¹, R. Farinelli^{24A,24B}, L. Fava^{58B,58C}, F. Feldbauer⁴, G. Felici^{23A}, C. Q. Feng^{55,43}, M. Fritsch⁴, C. D. Fu¹, Y. Fu¹, Q. Gao¹, X. L. Gao^{55,43}, Y. Gao⁵⁶, Y. Gao⁴⁵, Y. G. Gao⁶, Z. Gao^{55,43}, B. Garillon²⁶, I. Garzia^{24A}, E. M. Gersabeck⁵⁰, A. Gilman⁵¹, K. Goetzen¹¹, L. Gong³⁴, W. X. Gong^{1,43}, W. Gradl²⁶, M. Greco^{58A,58C}, L. M. Gu³³, M. H. Gu^{1,43}, S. Gu², Y. T. Gu¹³, A. Q. Guo²², L. B. Guo³², R. P. Guo³⁶, Y. P. Guo²⁶, A. Guskov²⁷, S. Han⁶⁰, X. Q. Hao¹⁶, F. A. Harris⁴⁸, K. L. He^{1,47}, F. H. Heinsius⁴, T. Held⁴, Y. K. Heng^{1,43,47}, M. Himmelreich^{11,g}, Y. R. Hou⁴⁷, Z. L. Hou¹, H. M. Hu^{1,47}, J. F. Hu^{38,h}, T. Hu^{1,43,47}, Y. Hu¹, G. S. Huang^{55,43}, J. S. Huang¹⁶, X. T. Huang³⁷, X. Z. Huang³³, N. Huesken⁵², T. Hussain⁵⁷, W. Ikegami Andersson⁵⁹, W. Imoehl²², M. Irshad^{55,43}, Q. Ji¹, Q. P. Ji¹⁶, X. B. Ji^{1,47}, X. L. Ji^{1,43}, H. L. Jiang³⁷, X. S. Jiang^{1,43,47}, X. Y. Jiang³⁴, J. B. Jiao³⁷, Z. Jiao¹⁸, D. P. Jin^{1,43,47}, S. Jin³³, Y. Jin⁴⁹, T. Johansson⁵⁹, N. Kalantar-Nayestanaki²⁹, X. S. Kang³¹, R. Kappert²⁹, M. Kavatsyuk²⁹, B. C. Ke¹, I. K. Keshk⁴, A. Khokkaz⁵², P. Kiese²⁶, R. Kiuchi¹, R. Klement¹¹, L. Koch²⁸, O. B. Kolcu^{46B,f}, B. Kopf⁴, M. Kuemmel⁴, M. Kuessner⁴, A. Kupsc⁵⁹, M. Kurth¹, M. G. Kurth^{1,47}, W. Kühn²⁸, J. S. Lange²⁸, P. Larin¹⁵, L. Lavezzi^{58C}, H. Leithoff²⁶, T. Lenz²⁶, C. Li⁵⁹, Cheng Li^{55,43}, D. M. Li⁶³, F. Li^{1,43}, F. Y. Li^{35,l}, G. Li¹, H. B. Li^{1,47}, H. J. Li^{9,j}, J. C. Li¹, J. W. Li⁴¹, Ke Li¹, L. K. Li¹, Lei Li^{3,53}, P. L. Li^{55,43}, P. R. Li³⁰, Q. Y. Li³⁷, W. D. Li^{1,47}, W. G. Li¹, X. H. Li^{55,43}, X. L. Li³⁷, X. N. Li^{1,43}, Z. B. Li⁴⁴, Z. Y. Li⁴⁴, H. Liang^{55,43}, H. Liang^{1,47}, Y. F. Liang⁴⁰, Y. T. Liang²⁸, G. R. Liao¹², L. Z. Liao^{1,47}, J. Libby²¹, C. X. Lin⁴⁴, D. X. Lin¹⁵, Y. J. Lin¹³, B. Liu^{38,h}, B. J. Liu¹, C. X. Liu¹, D. Liu^{55,43}, D. Y. Liu^{38,h}, F. H. Liu³⁹, Fang Liu¹, Feng Liu⁶, H. B. Liu¹³, H. M. Liu^{1,47}, Huanhuan Liu¹, Huihui Liu¹⁷, J. B. Liu^{55,43}, J. Y. Liu^{1,47}, K. Liu¹, K. Y. Liu³¹, Ke Liu⁶, L. Y. Liu¹³, Q. Liu⁴⁷, S. B. Liu^{55,43}, T. Liu^{1,47}, X. Liu³⁰, X. Y. Liu^{1,47}, Y. B. Liu³⁴, Z. A. Liu^{1,43,47}, Zhiqing Liu³⁷, Y. F. Long^{35,l}, X. C. Lou^{1,43,47}, H. J. Lu¹⁸, J. D. Lu^{1,47}, J. G. Lu^{1,43}, Y. Lu¹, Y. P. Lu^{1,43}, C. L. Luo³², M. X. Luo⁶², P. W. Luo⁴⁴, T. Luo^{9,j}, X. L. Luo^{1,43}, S. Lusso^{58C}, X. R. Lyu⁴⁷, F. C. Ma³¹, H. L. Ma¹, L. L. Ma³⁷, M. M. Ma^{1,47}, Q. M. Ma¹, X. N. Ma³⁴, X. X. Ma^{1,47}, X. Y. Ma^{1,43}, Y. M. Ma³⁷, F. E. Maas¹⁵, M. Maggiora^{58A,58C}, S. Maldaner²⁶, S. Malde⁵³, Q. A. Malik⁵⁷, A. Mangoni^{23B}, Y. J. Mao^{35,l}, Z. P. Mao¹, S. Marcello^{58A,58C}, Z. X. Meng⁴⁹, J. G. Messchendorp²⁹, G. Mezzadri^{24A}, J. Min^{1,43}, T. J. Min³³, R. E. Mitchell²², X. H. Mo^{1,43,47}, Y. J. Mo⁶, C. Morales Morales¹⁵, N. Yu. Muchnoi^{10,d}, H. Muramatsu⁵¹, A. Mustafa⁴, S. Nakhoul^{11,g}, Y. Nefedov²⁷, F. Nerling^{11,g}, I. B. Nikolaev^{10,d}, Z. Ning^{1,43}, S. Nisar^{8,k}, S. L. Niu^{1,43}, S. L. Olsen⁴⁷, Q. Ouyang^{1,43,47}, S. Pacetti^{23B}, Y. Pan^{55,43}, M. Papenbrock⁵⁹, P. Patteri^{23A}, M. Pelizaeus⁴, H. P. Peng^{55,43}, K. Peters^{11,g}, J. Pettersson⁵⁹, J. L. Ping³², R. G. Ping^{1,47}, A. Pitka⁴, R. Poling⁵¹, V. Prasad^{55,43}, H. R. Qi², M. Qi³³, T. Y. Qi², S. Qian^{1,43}, C. F. Qiao⁴⁷, N. Qin⁶⁰, X. P. Qin¹³, X. S. Qin⁴, Z. H. Qin^{1,43}, J. F. Qiu¹, S. Q. Qu³⁴, K. H. Rashid^{57,i}, K. Ravindran²¹, C. F. Redmer²⁶, M. Richter⁴, A. Rivetti^{58C}, V. Rodin²⁹, M. Rolo^{58C}, G. Rong^{1,47}, Ch. Rosner¹⁵, M. Rump⁵², A. Sarantsev^{27,e}, M. Savrié^{24B}, Y. Schelhaas²⁶, K. Schoenning⁵⁹, W. Shan¹⁹, X. Y. Shan^{55,43}, M. Shao^{55,43}, C. P. Shen², P. X. Shen³⁴, X. Y. Shen^{1,47}, H. Y. Sheng¹, X. Shi^{1,43}, X. D. Shi^{55,43}, J. J. Song³⁷, Q. Q. Song^{55,43}, X. Y. Song¹, S. Sosio^{58A,58C}, C. Sowa⁴, S. Spataro^{58A,58C}, F. F. Sui³⁷, G. X. Sun¹, J. F. Sun¹⁶, L. Sun⁶⁰, S. S. Sun^{1,47}, X. H. Sun¹, Y. J. Sun^{55,43}, Y. K. Sun^{55,43}, Y. Z. Sun¹, Z. J. Sun^{1,43}, Z. T. Sun¹, Y. T. Tan^{55,43}, C. J. Tang⁴⁰, G. Y. Tang¹, X. Tang¹, V. Thoren⁵⁹, B. Tsednee²⁵, I. Uman^{46D}, B. Wang¹, B. L. Wang⁴⁷, C. W. Wang³³, D. Y. Wang^{35,l}, K. Wang^{1,43}, L. L. Wang¹, L. S. Wang¹, M. Wang³⁷, M. Z. Wang^{35,l}, Meng Wang^{1,47}, P. L. Wang¹, R. M. Wang⁶¹, W. P. Wang^{55,43}, X. Wang^{35,l}, X. F. Wang¹, X. L. Wang^{9,j}, Y. Wang^{55,43}, Y. Wang⁴⁴, Y. F. Wang^{1,43,47}, Y. Q. Wang¹, Z. Wang^{1,43}, Z. G. Wang^{1,43}, Z. Y. Wang¹, Zongyuan Wang^{1,47}, T. Weber⁴, D. H. Wei¹², P. Weidenkaff²⁶, H. W. Wen³², S. P. Wen¹, U. Wiedner⁴, G. Wilkinson⁵³, M. Wolke⁵⁹, L. H. Wu¹, L. J. Wu^{1,47}, Z. Wu^{1,43}, L. Xia^{55,43}, Y. Xia²⁰, S. Y. Xiao¹, Y. J. Xiao^{1,47}, Z. J. Xiao³², Y. G. Xie^{1,43}, Y. H. Xie⁶, T. Y. Xing^{1,47}, X. A. Xiong^{1,47}, Q. L. Xiu^{1,43}, G. F. Xu¹, J. J. Xu³³, L. Xu¹, Q. J. Xu¹⁴, W. Xu^{1,47}, X. P. Xu⁴¹, F. Yan⁵⁶, L. Yan^{58A,58C}, W. B. Yan^{55,43}, W. C. Yan², Y. H. Yan²⁰, H. J. Yang^{38,h}, H. X. Yang¹, L. Yang⁶⁰, R. X. Yang^{55,43}, S. L. Yang^{1,47}, Y. H. Yang³³, Y. X. Yang¹², Yifan Yang^{1,47}, Z. Q. Yang²⁰, M. Ye^{1,43}, M. H. Ye⁷, J. H. Yin¹, Z. Y. You⁴⁴, B. X. Yu^{1,43,47}, C. X. Yu³⁴, J. S. Yu²⁰, T. Yu⁵⁶, C. Z. Yuan^{1,47}, X. Q. Yuan^{35,l}, Y. Yuan¹, A. Yuncu^{46B,a}, A. A. Zafar⁵⁷, Y. Zeng²⁰, B. X. Zhang¹, B. Y. Zhang^{1,43}, C. C. Zhang¹, D. H. Zhang¹, H. H. Zhang⁴⁴, H. Y. Zhang^{1,43}, J. Zhang^{1,47}, J. L. Zhang⁶¹, J. Q. Zhang⁴, J. W. Zhang^{1,43,47}, J. Y. Zhang¹, J. Z. Zhang^{1,47}, K. Zhang^{1,47}, L. Zhang⁴⁵, L. Zhang³³, S. F. Zhang³³, T. J. Zhang³³, X. Y. Zhang³⁷, Y. Zhang^{55,43}, Y. Zhang^{55,43}, Y. H. Zhang^{1,43}, Y. T. Zhang^{55,43}, Yang Zhang¹, Yao Zhang¹, Yi Zhang^{9,j}, Yu Zhang⁴⁷, Z. H. Zhang⁶, Z. P. Zhang⁵⁵, Z. Y. Zhang⁶⁰, G. Zhao¹, J. W. Zhao^{1,43}, J. Y. Zhao^{1,47}, J. Z. Zhao^{1,43}, Lei Zhao^{55,43}, Ling Zhao¹, M. G. Zhao³⁴, Q. Zhao¹, S. J. Zhao⁶³, T. C. Zhao¹, Y. B. Zhao^{1,43}, Z. G. Zhao^{55,43}, A. Zhemchugov^{27,b}, B. Zheng⁵⁶, J. P. Zheng^{1,43}, Y. Zheng^{35,l}, Y. H. Zheng⁴⁷, B. Zhong³², L. Zhou^{1,43}, L. P. Zhou^{1,47}, Q. Zhou^{1,47}, X. Zhou⁶⁰, X. K. Zhou⁴⁷, X. R. Zhou^{55,43}, Xiaoyu Zhou²⁰, Xu Zhou²⁰, A. N. Zhu^{1,47}, J. Zhu³⁴, J. Zhu⁴⁴, K. Zhu¹, K. J. Zhu^{1,43,47}, S. H. Zhu⁵⁴, W. J. Zhu³⁴, X. L. Zhu⁴⁵, Y. C. Zhu^{55,43}, Y. S. Zhu^{1,47}, Z. A. Zhu^{1,47}, J. Zhuang^{1,43}, B. S. Zou¹, J. H. Zou¹

(BESIII Collaboration)

¹ Institute of High Energy Physics, Beijing 100049, People's Republic of China² Beihang University, Beijing 100191, People's Republic of China³ Beijing Institute of Petrochemical Technology, Beijing 102617, People's Republic of China⁴ Bochum Ruhr-University, D-44780 Bochum, Germany⁵ Carnegie Mellon University, Pittsburgh, Pennsylvania 15213, USA⁶ Central China Normal University, Wuhan 430079, People's Republic of China⁷ China Center of Advanced Science and Technology, Beijing 100190, People's Republic of China

- ⁸ COMSATS University Islamabad, Lahore Campus, Defence Road, Off Raiwind Road, 54000 Lahore, Pakistan
- ⁹ Fudan University, Shanghai 200443, People's Republic of China
- ¹⁰ G.I. Budker Institute of Nuclear Physics SB RAS (BINP), Novosibirsk 630090, Russia
- ¹¹ GSI Helmholtzcentre for Heavy Ion Research GmbH, D-64291 Darmstadt, Germany
- ¹² Guangxi Normal University, Guilin 541004, People's Republic of China
- ¹³ Guangxi University, Nanning 530004, People's Republic of China
- ¹⁴ Hangzhou Normal University, Hangzhou 310036, People's Republic of China
- ¹⁵ Helmholtz Institute Mainz, Johann-Joachim-Becher-Weg 45, D-55099 Mainz, Germany
- ¹⁶ Henan Normal University, Xixiang 453007, People's Republic of China
- ¹⁷ Henan University of Science and Technology, Luoyang 471003, People's Republic of China
- ¹⁸ Huangshan College, Huangshan 245000, People's Republic of China
- ¹⁹ Hunan Normal University, Changsha 410081, People's Republic of China
- ²⁰ Hunan University, Changsha 410082, People's Republic of China
- ²¹ Indian Institute of Technology Madras, Chennai 600036, India
- ²² Indiana University, Bloomington, Indiana 47405, USA
- ²³ (A)INFN Laboratori Nazionali di Frascati, I-00044, Frascati, Italy; (B)INFN and University of Perugia, I-06100, Perugia, Italy
- ²⁴ (A)INFN Sezione di Ferrara, I-44122, Ferrara, Italy; (B)University of Ferrara, I-44122, Ferrara, Italy
- ²⁵ Institute of Physics and Technology, Peace Ave. 54B, Ulaanbaatar 13330, Mongolia
- ²⁶ Johannes Gutenberg University of Mainz, Johann-Joachim-Becher-Weg 45, D-55099 Mainz, Germany
- ²⁷ Joint Institute for Nuclear Research, 141980 Dubna, Moscow region, Russia
- ²⁸ Justus-Liebig-Universitaet Giessen, II. Physikalisches Institut, Heinrich-Buff-Ring 16, D-35392 Giessen, Germany
- ²⁹ KVI-CART, University of Groningen, NL-9747 AA Groningen, The Netherlands
- ³⁰ Lanzhou University, Lanzhou 730000, People's Republic of China
- ³¹ Liaoning University, Shenyang 110036, People's Republic of China
- ³² Nanjing Normal University, Nanjing 210023, People's Republic of China
- ³³ Nanjing University, Nanjing 210093, People's Republic of China
- ³⁴ Nankai University, Tianjin 300071, People's Republic of China
- ³⁵ Peking University, Beijing 100871, People's Republic of China
- ³⁶ Shandong Normal University, Jinan 250014, People's Republic of China
- ³⁷ Shandong University, Jinan 250100, People's Republic of China
- ³⁸ Shanghai Jiao Tong University, Shanghai 200240, People's Republic of China
- ³⁹ Shanxi University, Taiyuan 030006, People's Republic of China
- ⁴⁰ Sichuan University, Chengdu 610064, People's Republic of China
- ⁴¹ Soochow University, Suzhou 215006, People's Republic of China
- ⁴² Southeast University, Nanjing 211100, People's Republic of China
- ⁴³ State Key Laboratory of Particle Detection and Electronics, Beijing 100049, Hefei 230026, People's Republic of China
- ⁴⁴ Sun Yat-Sen University, Guangzhou 510275, People's Republic of China
- ⁴⁵ Tsinghua University, Beijing 100084, People's Republic of China
- ⁴⁶ (A)Ankara University, 06100 Tandogan, Ankara, Turkey; (B)Istanbul Bilgi University, 34060 Eyup, Istanbul, Turkey; (C)Uludag University, 16059 Bursa, Turkey; (D)Near East University, Nicosia, North Cyprus, Mersin 10, Turkey
- ⁴⁷ University of Chinese Academy of Sciences, Beijing 100049, People's Republic of China
- ⁴⁸ University of Hawaii, Honolulu, Hawaii 96822, USA
- ⁴⁹ University of Jinan, Jinan 250022, People's Republic of China
- ⁵⁰ University of Manchester, Oxford Road, Manchester, M13 9PL, United Kingdom
- ⁵¹ University of Minnesota, Minneapolis, Minnesota 55455, USA
- ⁵² University of Muenster, Wilhelm-Klemm-Str. 9, 48149 Muenster, Germany
- ⁵³ University of Oxford, Keble Road, Oxford, UK OX13RH
- ⁵⁴ University of Science and Technology Liaoning, Anshan 114051, People's Republic of China
- ⁵⁵ University of Science and Technology of China, Hefei 230026, People's Republic of China
- ⁵⁶ University of South China, Hengyang 421001, People's Republic of China
- ⁵⁷ University of the Punjab, Lahore-54590, Pakistan
- ⁵⁸ (A)University of Turin, I-10125, Turin, Italy; (B)University of Eastern Piedmont, I-15121, Alessandria, Italy; (C)INFN, I-10125, Turin, Italy
- ⁵⁹ Uppsala University, Box 516, SE-75120 Uppsala, Sweden
- ⁶⁰ Wuhan University, Wuhan 430072, People's Republic of China
- ⁶¹ Xinyang Normal University, Xinyang 464000, People's Republic of China
- ⁶² Zhejiang University, Hangzhou 310027, People's Republic of China
- ⁶³ Zhengzhou University, Zhengzhou 450001, People's Republic of China

^a Also at Bogazici University, 34342 Istanbul, Turkey

^b Also at the Moscow Institute of Physics and Technology, Moscow 141700, Russia

^c Also at the Functional Electronics Laboratory, Tomsk State University, Tomsk, 634050, Russia

^d Also at the Novosibirsk State University, Novosibirsk, 630090, Russia

^e Also at the NRC "Kurchatov Institute", PNPI, 188300, Gatchina, Russia

^f Also at Istanbul Arel University, 34295 Istanbul, Turkey

^g Also at Goethe University Frankfurt, 60323 Frankfurt am Main, Germany

^h Also at Key Laboratory for Particle Physics, Astrophysics and Cosmology, Ministry of Education; Shanghai Key Laboratory for Particle Physics and Cosmology; Institute of Nuclear and Particle Physics, Shanghai 200240, People's Republic of China

ⁱ Also at Government College Women University, Sialkot - 51310. Punjab, Pakistan.

^j Also at Key Laboratory of Nuclear Physics and Ion-beam Application (MOE) and Institute of Modern Physics, Fudan University, Shanghai 200443, People's Republic of China

^k Also at Harvard University, Department of Physics, Cambridge, MA, 02138, USA

^l Also at State Key Laboratory of Nuclear Physics and Technology, Peking University, Beijing 100871, People's Republic of China

Crucial inputs for a variety of CP -violation studies can be determined through the analysis of pairs of quantum-entangled neutral D mesons, which are produced in the decay of the $\psi(3770)$ resonance. The relative strong-phase parameters between D^0 and \bar{D}^0 in the decays $D^0 \rightarrow K_{S,L}^0 \pi^+ \pi^-$ are studied using 2.93 fb^{-1} of e^+e^- annihilation data delivered by the BEPCII collider and collected by the BESIII detector at a center-of-mass energy of 3.773 GeV. Results are presented in regions of the phase space of the decay. These are the most precise measurements to date of the strong-phase parameters in $D \rightarrow K_{S,L}^0 \pi^+ \pi^-$ decays. Using these parameters, the associated uncertainty on the Cabibbo-Kobayashi-Maskawa angle γ/ϕ_3 is expected to be between 0.7° and 1.2° , for an analysis using the decay $B^\pm \rightarrow DK^\pm$, $D \rightarrow K_S^0 \pi^+ \pi^-$, where D represents a superposition of D^0 and \bar{D}^0 states. This is a factor of three smaller than that achievable with previous measurements. Furthermore, these results provide valuable input for charm-mixing studies, other measurements of CP violation, and the measurement of strong-phase parameters for other D -decay modes.

PACS numbers: 13.25.Ft, 14.40.Lb, 14.65.Dw

I. INTRODUCTION

The study of quantum-correlated charm-meson pairs produced at threshold allows unique access to hadronic decay properties that are of great interest across a wide range of physics applications. In particular, determination of the strong-phase parameters provides vital input to measurements of the Cabibbo-Kobayashi-Maskawa (CKM) [1] angle γ (also denoted ϕ_3) and other CP -violating observables. The same parameters are required for studies of $D^0\bar{D}^0$ mixing and CP violation in charm at experiments above threshold. The angle γ is a parameter of the unitarity triangle (UT), which is a geometrical representation of the CKM matrix in the complex plane. Within the standard model (SM) all measurements of unitarity-triangle parameters should be self-consistent. The parameter γ is of particular interest since it is the only angle of the UT that can easily be extracted in tree-level processes, in which the contribution of non-SM effects is expected to be very small [2]. Therefore, a measurement of γ provides a benchmark of the SM with negligible theoretical uncertainties. A precise measurement of γ is an essential ingredient in testing the SM description of CP violation. A comparison between this, direct, measurement of gamma, and the indirect determination coming from the other constraints of the UT is a sensitive probe for new physics.

One of the most sensitive decay channels for measuring γ is $B^- \rightarrow DK^-, D \rightarrow K_S^0 \pi^+ \pi^-$ [4] where D represents a superposition of D^0 and \bar{D}^0 mesons. Throughout this paper, charge conjugation is assumed unless otherwise explicitly noted. The amplitude of the B^- decay can be written as

$$f_{B^-}(m_+^2, m_-^2) \propto f_D(m_+^2, m_-^2) + r_B e^{i(\delta_B - \gamma)} f_{\bar{D}}(m_+^2, m_-^2). \quad (1)$$

Here, m_+^2 and m_-^2 are the squared invariant masses of the $K_S^0 \pi^+$ and $K_S^0 \pi^-$ pairs from the $D^0 \rightarrow K_S^0 \pi^+ \pi^-$ decay, $f_D(m_+^2, m_-^2)$ ($f_{\bar{D}}(m_+^2, m_-^2)$) is the amplitude of the D^0 (\bar{D}^0) decay to $K_S^0 \pi^+ \pi^-$ at (m_+^2, m_-^2) in the Dalitz plot, r_B is the

ratio of the suppressed amplitude to the favored amplitude, and δ_B is the CP -conserving strong-phase difference between them. If the small second-order effects of charm mixing and CP violation [4–8] are ignored Eq. (1) can be written as

$$f_{B^-}(m_+^2, m_-^2) \propto f_D(m_+^2, m_-^2) + r_B e^{i(\delta_B - \gamma)} f_D(m_-^2, m_+^2) \quad (2)$$

through the use of the relation $f_{\bar{D}}(m_+^2, m_-^2) = f_D(m_-^2, m_+^2)$. The square of the amplitude clearly depends on the strong-phase difference $\Delta\delta_D \equiv \delta_D(m_+^2, m_-^2) - \delta_D(m_-^2, m_+^2)$, where $\delta_D(m_+^2, m_-^2)$ is the strong phase of $f_D(m_+^2, m_-^2)$. While the strong-phase difference can be inferred from an amplitude model of the decay $D^0 \rightarrow K_S^0 \pi^+ \pi^-$, such an approach introduces model-dependence in the measurement. This property is undesirable as the systematic uncertainty associated with the model is difficult to estimate reliably, since common approaches to amplitude-model building break the optical theorem [9]. Instead, the strong-phase differences may be measured directly in the decays of quantum-correlated neutral D meson pairs created in the decay of the $\psi(3770)$ resonance [4, 7]. This approach ensures a model-independent [10–14] measurement of γ where the uncertainty in the strong-phase knowledge can be reliably propagated.

Knowledge of the strong-phase difference in $D \rightarrow K_S^0 \pi^+ \pi^-$ has important applications beyond the measurement of the angle γ in $B^\pm \rightarrow DK^\pm$ decays. First, this information can be used in γ measurements based on other B decays [12, 15]. Second, it can be exploited to provide a model-independent measurement of the CKM angle β through a time-dependent analysis of $\bar{B}^0 \rightarrow Dh^0$ where h is a light meson [16] and $B^0 \rightarrow D\pi^+\pi^-$ [17]. Finally, $D \rightarrow K_S^0 \pi^+ \pi^-$ is also a powerful decay mode for performing precision measurements of oscillation parameters and CP violation in $D^0\bar{D}^0$ mixing [18–21]. Again, knowledge of the strong-phase differences allows these measurements to be executed in a model-independent manner [20, 21]. The ability to have model-independent results is critical as these mea-

measurements become increasingly precise with the large data sets that will be analyzed at LHCb and Belle II, over the coming decade.

The strong-phase differences in $D \rightarrow K_S^0 \pi^+ \pi^-$ have been studied by the CLEO collaboration using 0.82 fb^{-1} of data [22, 23]. These measurements are limited by their statistical precision and would contribute major uncertainties to the measurements of γ , and mixing and CP violation in the charm sector, anticipated in the near future. The BESIII detector at the BEPCII collider has the largest data sample collected at the $\psi(3770)$ resonance, corresponding to an integrated luminosity of 2.93 fb^{-1} . Therefore it is possible to substantially improve the knowledge of the strong-phase differences, which will reduce the associated uncertainty when used in other CP violation measurements.

The observables measured in this analysis are the amplitude-weighted average cosine and sine of the strong-phase difference for $D \rightarrow K_S^0 \pi^+ \pi^-$ and $D \rightarrow K_L^0 \pi^+ \pi^-$ in regions of phase space. The paper is organized as follows. In Sec. II the formalism of how the strong-phase information can be accessed is discussed along with the description of the phase space regions. The BESIII detector and the simulated data are described in Sec. III. The event selection is presented in Sec. IV. Sections V and VI describe the measurement of the strong-phase parameters and their systematic uncertainties. The impact of these results on measurements of γ is assessed in Sec. VII. This paper is accompanied by a letter submitted to Physical Review Letters [24].

II. FORMALISM

A. Division of phase space

The analysis of the data is performed in regions of phase space. Measurements are presented in three schemes which are identical to those used in Ref. [23]. All schemes divide the phase space into eight pairs of bins, symmetrically along the $m_+^2 = m_-^2$ line. The bins are indexed with i , running from -8 to 8 excluding zero. The bins have a positive index if their position satisfies $m_+^2 < m_-^2$, and the exchange of coordinates $(m_+^2, m_-^2) \leftrightarrow (m_-^2, m_+^2)$, changes the sign of the bin. The choice of division of the phase space has an impact on the sensitivity of the CP violation measurements that use this strong-phase information as input. The schemes are irregular in shape and are shown in Fig. 1. Detailed information on the choice of these regions is given in Ref. [23]. The scheme denoted “equal binning” defines regions such that the variation in $\Delta\delta_D$ over each bin is minimized, and is based on a model developed on flavor-tagged data [25] to partition the phase space. In the half of the Dalitz plot $m_+^2 < m_-^2$, the i th bin is defined by the condition

$$2\pi(i - 3/2)/8 < \Delta\delta_D(m_+^2, m_-^2) < 2\pi(i - 1/2)/8. \quad (3)$$

A more sensitive scheme for the measurement of γ , denoted as “optimal binning”, takes into account both the model of the $D^0 \rightarrow K_S^0 \pi^+ \pi^-$ decay and the expected distribution of

D decays arising from the process $B^- \rightarrow DK^-$ when determining the bins. This choice improves the sensitivity of γ measurements compared to the equal binning by approximately 10%. The third binning scheme, denoted the “modified optimal binning” is useful in analyzing samples with low yields [12]. Although these three binning schemes are based on the $D^0 \rightarrow K_S^0 \pi^+ \pi^-$ model reported in Ref. [25], this procedure does not introduce model-dependence into the analyses that employ the resulting strong-phase measurements. The determination of CP violation parameters will remain unbiased, but they may have a loss in sensitivity with respect to expectation, due to the differences between the model and the true strong-phase variation.

B. Event yields in quantum-correlated data

The interference between the amplitudes of the D^0 and \bar{D}^0 decays can be parameterized by two quantities c_i and s_i , which are the amplitude-weighted averages of $\cos\Delta\delta_D$ and $\sin\Delta\delta_D$ over each Dalitz plot bin. They are defined as

$$c_i = \frac{1}{\sqrt{F_i F_{-i}}} \int_i |f_D(m_+^2, m_-^2)| |f_D(m_-^2, m_+^2)| \times \cos[\Delta\delta_D(m_+^2, m_-^2)] dm_+^2 dm_-^2, \quad (4)$$

and

$$s_i = \frac{1}{\sqrt{F_i F_{-i}}} \int_i |f_D(m_+^2, m_-^2)| |f_D(m_-^2, m_+^2)| \times \sin[\Delta\delta_D(m_+^2, m_-^2)] dm_+^2 dm_-^2, \quad (5)$$

where F_i is the fraction of events found in the i th bin of the flavor-specific decay $D^0 \rightarrow K_S^0 \pi^+ \pi^-$.

The $\psi(3770)$ has a $C = -1$ quantum number and this is conserved in the strong decay in which two neutral D mesons are produced. Hence the two neutral D mesons have an anti-symmetric wave function. This also means that the two D mesons do not decay independently of one another.

For example, if one D meson decays to a CP -even eigenstate, e.g. $K^+ K^-$, then the other D meson is known to be a CP -odd state. The analysis strategy is to use double-tagged events in which both charm mesons are reconstructed. The yield of events in which one meson is flavor-tagged, e.g. through the decay $K^- e^+ \nu_e$, and the other decays to $D^0 \rightarrow K_S^0 \pi^+ \pi^-$ in bin i can be used to determine $K_i \propto \int_i |f_D(m_+^2, m_-^2)|^2 dm_+^2 dm_-^2$ [7]. The details of determining K_i through using flavor-specific decays are described in Sec. VB.

Considering a pair of decays where one D meson decays to CP eigenstate, referred to as “the tag”, and the other D meson decays to the $K_S^0 \pi^+ \pi^-$ final state, the decay amplitude of the $D \rightarrow K_S^0 \pi^+ \pi^-$ decay is given by

$$f_{CP\pm}(m_+^2, m_-^2) = \frac{1}{\sqrt{2}} [f_D(m_+^2, m_-^2) \pm f_D(m_-^2, m_+^2)], \quad (6)$$

where $f_{CP\pm}$ refers to the CP eigenvalue of the $D \rightarrow K_S^0 \pi^+ \pi^-$ decay. It is possible to generalize this expression

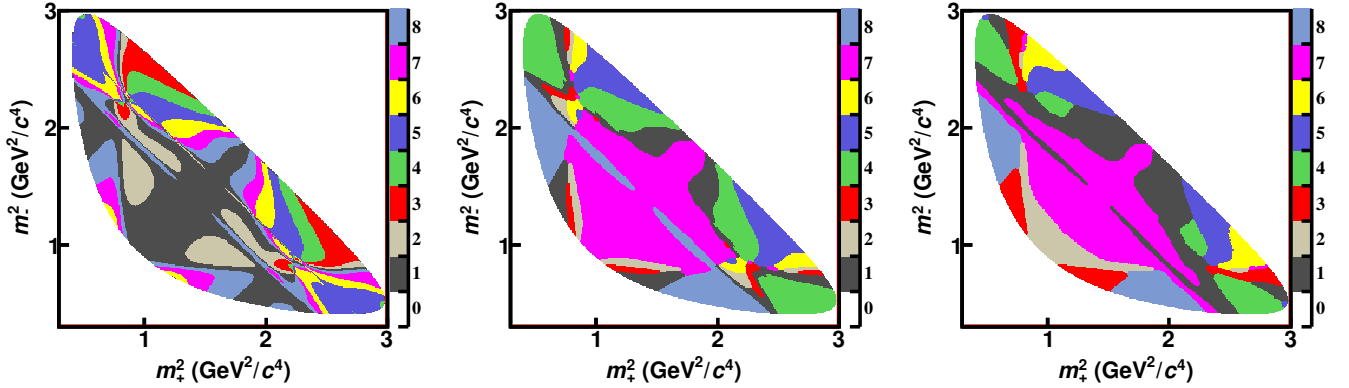


FIG. 1. The (left) equal $\Delta\delta_D$, (middle) optimal and (right) modified optimal binnings of the $D \rightarrow K_{S,L}^0\pi^+\pi^-$ Dalitz plot from Ref. [23]. The color scale represents the absolute value of the bin number $|i|$.

to include decays where the tag D meson decays to a self-conjugate final state rather than a CP eigenstate, assuming that the CP -even fraction, F_{CP} , is known. The number of events observed in the i th bin, M_i , where the tag D meson decays to a self-conjugate final state is then given by

$$M_i = h_{CP}(K_i - (2F_{CP} - 1)2c_i\sqrt{K_i K_{-i}} + K_{-i}), \quad (7)$$

where h_{CP} is a normalization factor. The value of F_{CP} is 1 for CP -even tags and 0 for CP -odd tags. This parameterization is valuable since it allows for final states with very high or very low CP -even fractions to be used to provide sensitivity to the c_i parameters. A good example of such a decay is the mode $D \rightarrow \pi^+\pi^-\pi^0$ where the fractional CP -even content is measured to be $F_{CP}^{\pi\pi\pi^0} = 0.973 \pm 0.017$ [26].

However, from Eq. (4), the sign of $\Delta\delta_D$ is undetermined if only the values of c_i are known from the CP -tagged $D \rightarrow K_S^0\pi^+\pi^-$ decay. Important additional information can be gained to determine the s_i parameters by studying the Dalitz plot distributions where both D mesons decay to $K_S^0\pi^+\pi^-$. The amplitude of the $\psi(3770)$ decay is in this case given by

$$f(m_+^2, m_-^2, m_+^{2\dagger}, m_-^{2\dagger}) = \frac{f_D(m_+^2, m_-^2)f_D(m_-^{2\dagger}, m_+^{2\dagger}) - f_D(m_+^{2\dagger}, m_-^{2\dagger})f_D(m_-^2, m_+^2)}{\sqrt{2}}, \quad (8)$$

where the use of the \dagger symbol differentiates the Dalitz plot coordinates of the two $D \rightarrow K_S^0\pi^+\pi^-$ decays. The variable M_{ij} is defined as the event yield observed in the i th bin of the first and the j th bin of the second $D \rightarrow K_S^0\pi^+\pi^-$ Dalitz plot, and is given by

$$M_{ij} = h_{\text{corr}}[K_i K_{-j} + K_{-i} K_j - 2\sqrt{K_i K_{-j} K_{-i} K_j}(c_i c_j + s_i s_j)], \quad (9)$$

where h_{corr} is a normalization factor. Equation (9) is not sensitive to the sign of s_i , however, this ambiguity can be resolved using a weak model assumption.

In order to improve the precision of the c_i and s_i parameters it is useful to increase the possible tags to include $D \rightarrow K_L^0\pi^+\pi^-$ which is closely related to the $D \rightarrow K_S^0\pi^+\pi^-$ decay. The convention $A(D^0 \rightarrow K_S^0\pi^+\pi^-) = A(\bar{D}^0 \rightarrow K_S^0\pi^-\pi^+)$ is used, making the good approximation that the K_S^0 meson is CP -even. Similarly, it follows that $A(D^0 \rightarrow K_L^0\pi^+\pi^-) = -A(\bar{D}^0 \rightarrow K_L^0\pi^-\pi^+)$. Hence, where the $D \rightarrow K_L^0\pi^+\pi^-$ is used as the signal decay, and the tag is a self-conjugate final state, the observed event yield M'_i is given by

$$M'_i = h'_{CP}(K'_i + (2F_{CP} - 1)2c'_i\sqrt{K'_i K'_{-i}} + K'_{-i}), \quad (10)$$

where K'_i and c'_i are associated to the $D \rightarrow K_L^0\pi^+\pi^-$ decay. The event yield M'_{ij} , corresponding to the yield of events where the $D \rightarrow K_S^0\pi^+\pi^-$ decay is observed in the i th bin and the $D \rightarrow K_L^0\pi^+\pi^-$ decay is observed in the j th bin, is given by

$$M'_{ij} = h'_{\text{corr}}[K_i K'_{-j} + K_{-i} K'_j + 2\sqrt{K_i K'_{-j} K_{-i} K'_j}(c_i c'_j + s_i s'_j)], \quad (11)$$

where s'_i is the amplitude-weighted average sine of the strong-phase difference for the $D \rightarrow K_L^0\pi^+\pi^-$ decay.

In Eqs. (7), (9), (10) and (11), the normalization factors $h_{CP}^{(\prime)}$ and $h_{\text{corr}}^{(\prime)}$ can be related to the yields of reconstructed signal and tag final states, the reconstruction efficiencies, and the number of neutral D -meson pairs $N_{D\bar{D}}$ produced in the data set, with $h_{CP}^{(\prime)} = S_{CP}/2S_{\text{FT}^{(\prime)}} \times \epsilon^{K_{S(L)}^0\pi^+\pi^-}$, $h_{\text{corr}} = N_{D\bar{D}}/(2S_{\text{FT}}^2) \times \epsilon^{K_S^0\pi^+\pi^- \text{ vs. } K_S^0\pi^+\pi^-}$ and $h'_{\text{corr}} = N_{D\bar{D}}/(S_{\text{FT}}S'_{\text{FT}}) \times \epsilon^{K_S^0\pi^+\pi^- \text{ vs. } K_L^0\pi^+\pi^-}$. Here S_{CP} is the yield of events in which one charm meson is reconstructed as the CP -tag where no requirement is placed on the decay of the other charm meson, and $S_{\text{FT}^{(\prime)}}$ refers to the analogous quantity summed over flavor-tagged decays that are used in the determination of $K_i^{(\prime)}$. The effective efficiency for detecting the $D \rightarrow K_{S(L)}^0\pi^+\pi^-$ decay recoiling against the particular CP -tag under consideration, is defined

as $\epsilon^{K_{S(L)}^0\pi^+\pi^-} = \epsilon_{\text{DT}}/\epsilon_{\text{ST}}$, where ϵ_{ST} is the detection efficiency for finding the CP -tagged candidate, while ϵ_{DT} is the efficiency for simultaneously finding the CP -tagged candidate and the signal decay $D \rightarrow K_{S(L)}^0\pi^+\pi^-$. Furthermore, $\epsilon^{K_S^0\pi^+\pi^- \text{ vs. } K_S^0\pi^+\pi^-}$ and $\epsilon^{K_S^0\pi^+\pi^- \text{ vs. } K_L^0\pi^+\pi^-}$ are efficiencies for detecting $D \rightarrow K_S^0\pi^+\pi^-$ vs. $D \rightarrow K_S^0\pi^+\pi^-$ and $D \rightarrow K_L^0\pi^+\pi^-$ vs. $D \rightarrow K_S^0\pi^+\pi^-$, respectively. Note that, as is discussed in Sec. VB, finite detector resolution results in the migration of reconstructed events between Dalitz plot bins. In order to avoid biases arising from these migration effects it is necessary to modify Eqs. (7), (9), (10) and (11) by substituting the efficiencies in the normalization factors $h_{CP}^{(i)}$ and $h_{\text{corr}}^{(i)}$ by efficiency matrices, as described in Sec. VC.

III. THE BESIII DETECTOR

BEPCII is a double-ring e^+e^- collider with a center-of-mass energy ranging from 2 to 5 GeV and a design luminosity of $10^{33} \text{ cm}^{-2}\text{s}^{-1}$ at a beam energy of 1.89 GeV. The BESIII detector at BEPCII is a cylindrical detector with a solid-angle coverage of 93% of 4π . The detector consists of a helium-gas based main drift chamber (MDC), a plastic scintillator time-of-flight (TOF) system, a CsI(Tl) electromagnetic calorimeter (EMC), a superconducting solenoid providing a 1.0 T magnetic field and a muon counter. The charged-particle momentum resolution is 0.5% at a transverse momentum of 1 GeV/ c , and the specific energy loss (dE/dx) resolution is 6% for the electrons from Bhabha scattering. The photon energy resolution in the EMC is 2.5% in the barrel and 5.0% in the end-caps at energies of 1 GeV. The time resolution of the TOF barrel part is 68 ps, while that of the end-cap part is 110 ps. More details about the design and performance of the detector are given in Ref. [27].

A GEANT4-based [28] simulation package, which includes the geometric description of the detector and the detector response, is used to determine signal detection efficiencies and to estimate potential backgrounds. The production of the $\psi(3770)$, initial-state radiation (ISR) production of the $\psi(2S)$ and J/ψ , and the continuum processes $e^+e^- \rightarrow \tau^+\tau^-$ and $e^+e^- \rightarrow q\bar{q}$ ($q = u, d$ and s) are simulated with the event generator KKMC [29], with the inclusion of ISR effects up to second-order corrections [30]. The final-state radiation effects are simulated via the PHOTOS package [31]. The known decay modes are generated by EVTGEN [32] with the branching fractions (BFs) set to the world average values from the Particle Data Group [33], while the remaining unknown decay modes are modeled by LUNDCHARM [34]. The generation of simulated signals $D^0 \rightarrow K_S^0\pi^+\pi^-$ and $D^0 \rightarrow K_L^0\pi^+\pi^-$ is based on the knowledge of isobar resonance amplitudes from the Dalitz plot analysis of $D^0 \rightarrow K_S^0\pi^+\pi^-$. The $D^0 \rightarrow \pi^+\pi^-\pi^0$ decay is simulated with a phase-space model since the relative contributions of intermediate resonances in the decay are poorly known. For other multibody decay modes the simulated data are based on amplitude models, where available, or through an estimate of the expected intermediate resonances participating in the decay.

TABLE I. A list of tag decay modes used in the analysis.

Tag group	
Flavor	$K^+\pi^-, K^+\pi^-\pi^0, K^+\pi^-\pi^-\pi^+, K^+e^-\bar{\nu}_e$
CP -even	$K^+K^-, \pi^+\pi^-, K_S^0\pi^0\pi^0, K_L^0\pi^0, \pi^+\pi^-\pi^0$
CP -odd	$K_S^0\pi^0, K_S^0\eta, K_S^0\omega, K_S^0\eta', K_L^0\pi^0\pi^0$
Mixed- CP	$K_S^0\pi^+\pi^-$

IV. EVENT SELECTION

In order to measure c_i, s_i, c'_i and s'_i , a range of single-tag (ST) and double-tag (DT) samples of D decays are reconstructed. The ST samples are those where the decay products of only one D meson are reconstructed. The DT samples are those where one D meson decays to the signal mode $K_S^0\pi^+\pi^-$ or $K_L^0\pi^+\pi^-$ and the other D meson decays to one of the tag modes listed in Table I. Tag decay modes fall into the categories of flavor, CP eigenstates or mixed- CP . Flavor tags identify the flavor of the decaying meson through a semi-leptonic decay or a Cabibbo-favored hadronic decay (contamination from doubly-Cabibbo-suppressed (DCS) decays is discussed later). CP eigenstates and mixed- CP tags identify a decay from an initial state which is a superposition of D^0 and \bar{D}^0 . The $D \rightarrow \pi^+\pi^-\pi^0$ tag is used for the first time to measure the strong-phase parameters in $D \rightarrow K_{S,L}^0\pi^+\pi^-$ decays. It has a relatively high BF and selection efficiency resulting in a large increase to the CP -tagged yields. The use of this tag is possible through the knowledge of F_{CP} for this decay [26]. In this paper the $D \rightarrow \pi^+\pi^-\pi^0$ is referred to as a CP -even eigenstate, although its small CP -odd component is always taken into account, as in Eq. (7).

Due to the hermetic nature of the detector it is possible to use missing energy and momentum constraints to infer the presence of the neutrino in the $K^+e^-\bar{\nu}_e$ final state that does not leave a response in the detector. Similarly, the K_L^0 meson, which does not decay within the detector, can be inferred by requiring the missing energy and momentum to be consistent with a K_L^0 particle. Tag decay modes such as $D \rightarrow K_L^0\omega$ are not included in the analysis as the systematic uncertainty due to the need to estimate their BFs would be larger than the impact on statistical precision brought from the increased CP -tag yields. The principles of missing energy and momentum can also be used to increase the selection efficiency in highly sensitive decay modes by only partially reconstructing the $D \rightarrow K_S^0\pi^+\pi^-$ candidate. The DT combinations that result in two missing particles are not pursued due to the inability to reliably allocate the missing energy and momentum between two missing particles. The ST yields are only measured in decay modes that are fully reconstructable.

In this paper, we use the following selection criteria to reconstruct the ST and DT samples. The charged tracks are required to be well reconstructed in the MDC detector with the polar angle θ satisfying $|\cos\theta| < 0.93$. Their distances of the closest approach to the interaction point (IP) are required to be less than 10 cm along the beam direction and less than 1 cm in the perpendicular plane. For tracks originating from

K_S^0 , their distances of closest approach to the IP are required to be within 20 cm along the beam direction.

To discriminate pions from kaons, the dE/dx and TOF information are used to obtain particle identification (PID) likelihoods for the pion (\mathcal{L}_π) and kaon (\mathcal{L}_K) hypotheses. Pion and kaon candidates are selected using $\mathcal{L}_\pi > \mathcal{L}_K$ and $\mathcal{L}_K > \mathcal{L}_\pi$, respectively. To identify the electron, the information measured by the dE/dx , TOF, and EMC are used to construct likelihoods for electron, pion and kaon hypotheses (\mathcal{L}'_e , \mathcal{L}'_π and \mathcal{L}'_K). The electron candidate must satisfy $\mathcal{L}'_e > 0.001$ and $\mathcal{L}'_e/(\mathcal{L}'_e + \mathcal{L}'_\pi + \mathcal{L}'_K) > 0.8$. K_S^0 mesons are reconstructed from two oppositely charged tracks with an invariant mass within (0.485, 0.510) GeV/ c^2 . A fit is applied to constrain these two charged tracks to a common vertex, and the decay vertex is required to be separated from the interaction point by more than twice the standard deviation (σ) of the measured flight distance (L), *i.e.*, $L/\sigma_L > 2$, in order to suppress the background from pion pairs that do not originate from a K_S^0 meson.

Photon candidates are reconstructed from isolated clusters in the EMC in the regions $|\cos\theta| \leq 0.80$ (barrel) and $0.86 \leq |\cos\theta| \leq 0.92$ (end cap). The deposited energy of a neutral cluster is required to be larger than 25 (50) MeV in barrel (end cap) region. To suppress electronic noise and energy deposits unrelated to the event, the difference between the EMC time and the event start time is required to be within (0, 700) ns. To reconstruct $\pi^0(\eta)$ candidates, the invariant mass of the accepted photon pair is required to be within (0.110, 0.155)[(0.48, 0.58)] GeV/ c^2 . To improve the momentum resolution, a kinematic fit is applied to constrain the $\gamma\gamma$ invariant mass to the nominal $\pi^0(\eta)$ mass [33], and the χ^2 of the kinematic fit is required to be less than 20. The fitted momenta of the $\pi^0(\eta)$ are used in the further analysis. When reconstructing η candidates decaying through $\eta \rightarrow \pi^+\pi^-\pi^0$, it is required that their invariant masses be within (0.530, 0.655) GeV/ c^2 . Similarly, ω candidates are selected by requiring the invariant mass of $\pi^+\pi^-\pi^0$ to be within (0.750, 0.820) GeV/ c^2 . The decay modes $\eta' \rightarrow \pi^+\pi^-\eta$ and $\eta' \rightarrow \gamma\pi^+\pi^-$ are used to reconstruct η' mesons, with the invariant masses of the $\pi^+\pi^-\eta$ and $\gamma\pi^+\pi^-$ required to be within (0.942, 0.973) and (0.935, 0.973) GeV/ c^2 , respectively.

A. Single-tag yields

The ST D signals are identified using the beam-constrained mass,

$$M_{\text{BC}} = \sqrt{(\sqrt{s}/2)^2 - |\vec{p}_{D_{\text{tag}}}|^2}, \quad (12)$$

where $\vec{p}_{D_{\text{tag}}}$ is the momentum of the D candidate. To improve the signal purity, the energy difference $\Delta E = \sqrt{s}/2 - E_{D_{\text{tag}}}$ for each candidate is required to be within approximately $\pm 3\sigma_{\Delta E}$ around the ΔE peak, where $\sigma_{\Delta E}$ is the ΔE resolution and $E_{D_{\text{tag}}}$ is the reconstructed ST D energy. The explicit ΔE requirements for all reconstructed ST modes are listed in the second column of Table II. If multiple combinations are selected, the one with the minimum $|\Delta E|$ is retained. For the ST channels of $K^+\pi^-$, K^+K^- and $\pi^+\pi^-$,

backgrounds of cosmic rays and Bhabha events are removed with the following requirements. First, the two charged tracks must have a TOF time difference of less than 5 ns and they must not be consistent with being a muon pair or an e^+e^- pair. Second, there must be at least one EMC shower with an energy larger than 50 MeV or at least one additional charged track detected in the MDC.

The M_{BC} distributions for the ST modes are shown in Fig. 2. To obtain the ST yields reconstructed by these modes, maximum likelihood fits are performed to these spectra, where the signal peak is described by a Monte Carlo (MC) simulated shape convolved with a double-Gaussian function, and the combinatorial background is modeled with an ARGUS function [35]. In addition to the combinatorial background, there are also some peaking backgrounds in the signal region of M_{BC} . These peaking backgrounds are included in the yields obtained from fits to M_{BC} spectra and hence must be subtracted. For example, for the ST modes of $K^+\pi^-$, $K^+\pi^-\pi^0$ and $K^+\pi^-\pi^-\pi^+$, there are small contributions of wrong-sign (WS) peaking backgrounds in the ST \bar{D}^0 samples, which originate from the DCS-dominated decays of $D^0 \rightarrow K^+\pi^-$, $K^+\pi^-\pi^0$ and $K^+\pi^-\pi^-\pi^+$. In addition, the $D^0 \rightarrow K_S^0 K^+\pi^-$ ($K_S^0 \rightarrow \pi^+\pi^-$) decay is a source of WS peaking background for the ST decay $\bar{D}^0 \rightarrow K^+\pi^-\pi^-\pi^+$. Overall, the peaking background contamination rates are less than 1% for the ST modes of $K^+\pi^-$, $K^+\pi^-\pi^0$ and $K^+\pi^-\pi^-\pi^+$. For the CP -eigenstate ST channels $K_S^0\pi^0(\pi^0)$ and $\pi^+\pi^-\pi^0$, the peaking background rates are 0.8%(3.9%) and 3.9%, dominated by the D meson decays to $\pi^+\pi^-\pi^0(\pi^0)$ and $K_S^0\pi^0$, respectively. The $D \rightarrow K_S^0\pi^+\pi^-\pi^0$ decay forms the dominant peaking backgrounds and accounts for contamination rates of 13.7%, 6.3% and 3.8% in the fitted ST yields for $K_S^0\omega$, $K_S^0\eta_{\pi^+\pi^-\pi^0}$ and $K_S^0\eta'_{\gamma\pi^+\pi^-}$, respectively. Additionally, the sample of ST $K_S^0\pi^+\pi^-$ decays includes a 2% contamination from the peaking-background $D \rightarrow \pi^+\pi^-\pi^+\pi^-$. The sizes of these peaking backgrounds are all estimated from MC simulation and then subtracted from the fitted ST yields. The background-subtracted yield and the efficiency for each of the ST modes are summarized in the third and fourth columns of Table II, respectively. The ST efficiencies are determined from the simulated data where one D meson is forced to decay to the reconstructed final states and the other D meson is allowed to decay to any final state. The values of ϵ_{ST} vary from $\sim 65\%$ for decay modes with two charged particles in the final state to $\sim 13\%$ for final states with multiple composite and neutral particles such as $K_S^0\eta'_{\pi^+\pi^-\eta}$.

The ST yields of the modes $K^+e^-\bar{\nu}_e$, $K_L^0\pi^0$ and $K_L^0\pi^0\pi^0$, which cannot be directly reconstructed, are estimated from knowledge of the number of neutral D meson pairs $N_{D\bar{D}}$, the estimated ST efficiencies $\epsilon_{\text{tag}}^{\text{ST}}$, and their BFs \mathcal{B}_{tag} reported in Ref. [33], where the $D \rightarrow K_S^0\pi^0\pi^0$ BF is used as a proxy for $D \rightarrow K_L^0\pi^0\pi^0$. The yields are calculated from the relations

$$N_{\text{tag}}^{\text{ST}} = 2N_{D\bar{D}} \times \mathcal{B}_{\text{tag}} \times \epsilon_{\text{tag}}^{\text{ST}}$$

where $N_{D\bar{D}} = (10597 \pm 28 \pm 98) \times 10^3$ [36]. The ST efficiencies, $\epsilon_{\text{tag}}^{\text{ST}}$, of detecting these three decays are estimated by evaluating the ratios between the corresponding DT (dis-

cussed later in Sec. IV F) and ST efficiencies, which are determined to be 61.35%, 48.97% and 26.20% for $D \rightarrow K^+ e^- \bar{\nu}_e$, $D \rightarrow K_L^0 \pi^0$ and $D \rightarrow K_L^0 \pi^0 \pi^0$, respectively. The ST yields of $D \rightarrow K^- e^+ \nu_e$, $D \rightarrow K_L^0 \pi^0$ and $D \rightarrow K_L^0 \pi^0 \pi^0$ are also included in Table II, in which the uncertainties from the BFs, $N_{D\bar{D}}$ and the detection efficiencies are presented.

B. Double tags with $K_S^0 \pi^+ \pi^-$

In those cases where the decay products of the tag mode are fully reconstructed and the signal mode is $D \rightarrow K_S^0 \pi^+ \pi^-$, the signal decay is built by using the other tracks in the event recoiling against the ST D meson. The same selection on track parameters and the K_S^0 candidate is imposed as described for the $D \rightarrow K_S^0 \pi^+ \pi^-$ ST case. The energy difference, $\Delta E' = \sqrt{s}/2 - E_{\text{sig}}$, where E_{sig} is the energy of the $D \rightarrow K_S^0 \pi^+ \pi^-$ candidate, is required to be between -30 and 33 MeV. If multiple combinations are selected, the one with the minimum $|\Delta E'|$ is retained. The beam-constrained mass is defined as $M_{\text{BC}}^{\text{sig}} = \sqrt{(\sqrt{s}/2)^2 - |\vec{p}_{\text{sig}}|^2}$, where \vec{p}_{sig} is the momentum of the signal-decay candidate.

The DT yield is determined by performing a two-dimensional unbinned maximum-likelihood fit to the $M_{\text{BC}}^{\text{sig}}$ (signal) vs. $M_{\text{BC}}^{\text{tag}}$ (tag) distribution. An example distribution for the tag mode $D \rightarrow K^+ \pi^-$ is shown in Fig. 3. The signal shape of the $M_{\text{BC}}^{\text{sig}}$ vs. $M_{\text{BC}}^{\text{tag}}$ distributions is modeled with a two-dimensional shape derived from simulated data convolved with two independent Gaussian functions representing the resolution differences between data and simulation. The parameters of the Gaussian functions are fixed at the values obtained from the one-dimensional fits of the $M_{\text{BC}}^{\text{sig}}$ and $M_{\text{BC}}^{\text{tag}}$ distributions in data, respectively. The combinatorial backgrounds in the $M_{\text{BC}}^{\text{sig}}$ and $M_{\text{BC}}^{\text{tag}}$ distributions are modeled by an ARGUS function in each dimension where the parameters are determined in the fit. The events that are observed along the diagonal arise from mis-reconstructed $D\bar{D}$ decays and from $q\bar{q}$ events. They are described with a product of a double-Gaussian function and an ARGUS function rotated by 45° [36]. The kinematic limit and exponent parameters of the rotated ARGUS function are fixed, while the slope parameter is determined by the fit. The peaking backgrounds in the $M_{\text{BC}}^{\text{sig}}$ and $M_{\text{BC}}^{\text{tag}}$ distributions are described by using a shape derived from simulation convolved with the same Gaussian function as used for the signal. The decay $D \rightarrow \pi^+ \pi^- \pi^+ \pi^-$, which accounts for about 2% peaking background to $D \rightarrow K_S^0 \pi^+ \pi^-$ signal, is predominantly CP -even [37], and hence the yields of this peaking background are adjusted from the expectation of simulation to account for the effects of quantum correlation. Figure 4 shows the projections of the two-dimensional fits on the $M_{\text{BC}}^{\text{sig}}$ distribution for all the fully reconstructed ST decay modes.

The DT yield of $K_S^0 \pi^+ \pi^-$ vs. $K_S^0 \pi^+ \pi^-$ is crucial for determining the s_i values and thus it is desirable to increase the reconstruction efficiency for these events. Therefore three independent selections are introduced in order to maximize the yield of $D \rightarrow K_S^0 \pi^+ \pi^-$ vs. $D \rightarrow K_S^0 \pi^+ \pi^-$ candidates.

The first selection requires that both $K_S^0 \pi^+ \pi^-$ final states on the signal and tag side are fully reconstructed. However, in order to increase the efficiency, the PID requirements on the pions originating from both the signal and tag D mesons are removed and the K_S^0 candidate needs only satisfy $L/\sigma_L > 0$ (i.e., only candidates where L is negative due to detector resolution are removed). This looser selection is applied to both D mesons and allows for an increase in yield of approximately 20% with only a slight increase in background.

The second selection class allows for one pion originating from the D meson to be unreconstructed in the MDC, denoted as $K_S^0 \pi^+ \pi_{\text{miss}}^-$. Events with only three remaining charged tracks recoiling against the $D \rightarrow K_S^0 \pi^+ \pi^-$ ST are searched for. The K_S^0 and pion are identified with the same criteria used to select the ST candidates. The missing pion is inferred by calculating the missing-mass squared (M_{miss}^2) of the event, which is defined as

$$M_{\text{miss}}^2 = (\sqrt{s}/2 - \sum_i E_i)^2 - |\vec{p}_{\text{sig}} - \sum_i \vec{p}_i|^2, \quad (13)$$

where \vec{p}_{sig} is the momentum of the fully reconstructed $D \rightarrow K_S^0 \pi^+ \pi^-$ candidate and $\sum_i E_i$ and $\sum_i \vec{p}_i$ are the sum of the energy and momentum of the other reconstructed particles that form the partially reconstructed D meson candidate. Throughout this paper, in order to determine the signal yields of the DT containing a missing particle, an unbinned maximum-likelihood fit is performed to the defined kinematic distribution, i.e. M_{miss}^2 (or U_{miss} discussed in Sec. IV D). The signal and background components are described using shapes from simulated data where the signal shape is further convolved with a Gaussian function. The relative yields of the peaking backgrounds to the signals are fixed in the fits from information of the simulated data. Figure 5(a) shows the M_{miss}^2 distribution from the partially reconstructed $D \rightarrow K_S^0 \pi^+ \pi^-$ vs. $D \rightarrow K_S^0 \pi^+ \pi_{\text{miss}}^-$ candidates. The distribution peaks at $M_{\text{miss}}^2 \sim 0.02 \text{ GeV}^2/c^4$, which is consistent with the missing particle being a π^\pm . The peaking backgrounds are approximately 3% of the signal yield and are primarily from the $D \rightarrow \pi^+ \pi^- \pi^+ \pi^-$ decay.

The third $D \rightarrow K_S^0 \pi^+ \pi^-$ vs. $D \rightarrow K_S^0 \pi^+ \pi^-$ selection identifies those events where one K_S^0 meson decays to a $\pi^0 \pi^0$ pair. Events where there are only two remaining oppositely-charged tracks recoiling against the ST $D \rightarrow K_S^0 \pi^+ \pi^-$ are selected and these tracks are classified as the π^+ and π^- from the D meson. To avoid the reduced efficiency associated with reconstructing both π^0 mesons from the K_S^0 , only one of the them is searched for. This type of tag is referred to as $K_S^0(\pi^0 \pi_{\text{miss}}^0) \pi^+ \pi^-$. The missing-mass squared of the event is defined in the same way as in Eq. (13) and the summation is over the π^+ , π^- , and π^0 mesons that are reconstructed on the tag side. A further variable, $M_{\text{miss}}^{\prime 2}$, where the reconstructed π^0 is also not included in the summed energies and momenta of the tag-side particles is also computed. For true $D \rightarrow K_S^0 \pi^+ \pi^-$ decays this variable should be consistent with the square of the K_S^0 meson nominal mass. Therefore, candidates that do not satisfy $0.22 < M_{\text{miss}}^{\prime 2} < 0.27 \text{ GeV}^2/c^4$ are removed from the analysis in order to suppress background from $D \rightarrow \pi^+ \pi^- \pi^0 \pi^0$ decays. Figure 5(b) shows the re-

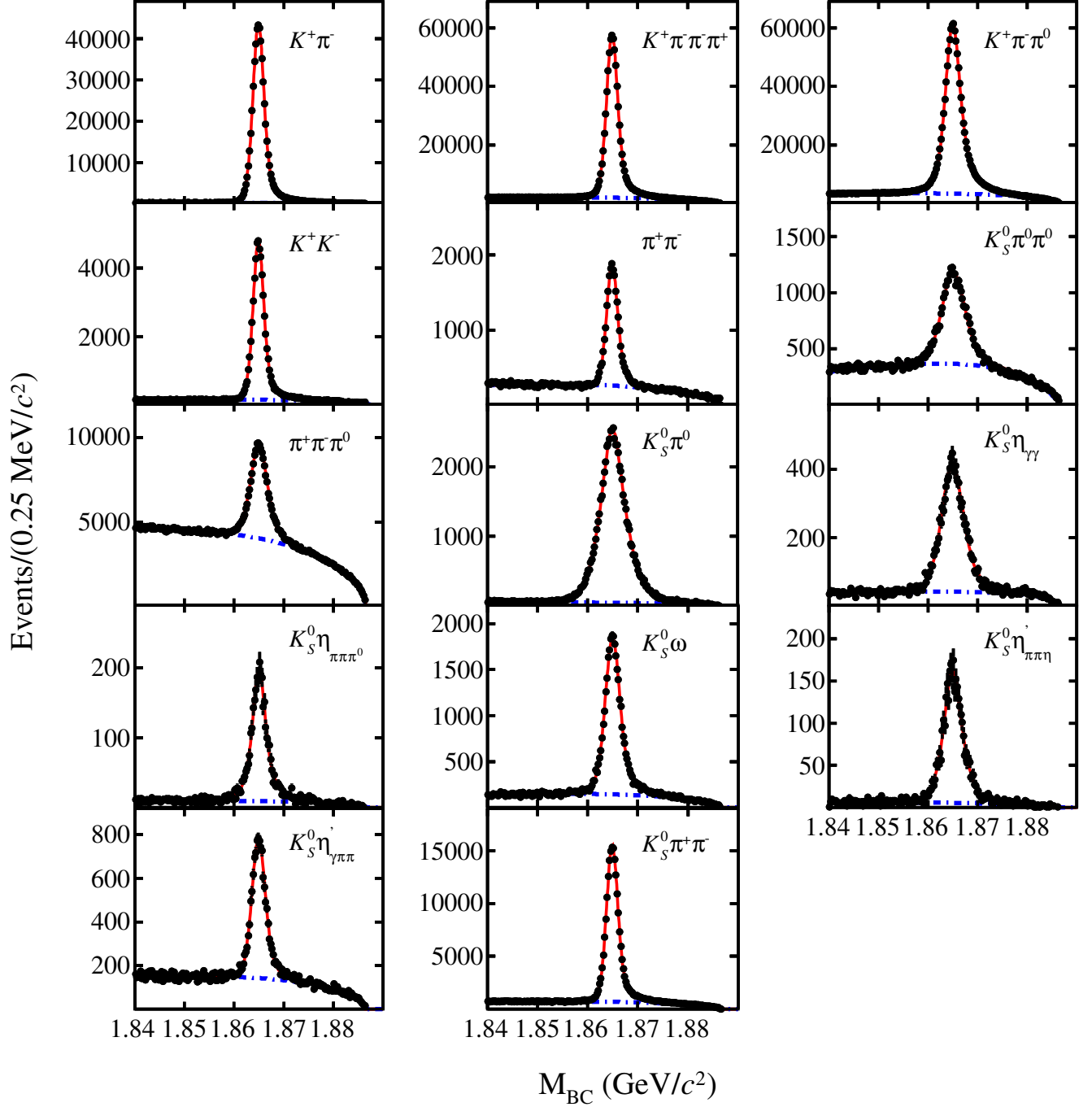


FIG. 2. Fits to M_{BC} distributions for the candidates for the ST decay modes as denoted by the labels on each plot. The black points represent data. Overlaid is the fit to data which is indicated by the continuous red line. The blue dashed line indicates the combinatorial background component of the fit.

sultant M_{miss}^2 distribution of the accepted candidates in data. There remains a contribution of peaking background dominated from $D \rightarrow \pi^+ \pi^- \pi^0 \pi^0$ decays, where the rate relative to signal is determined from simulated data to be around 15%.

C. Double tags with $K_L^0 \pi^0$ and $K_L^0 \pi^0 \pi^0$

The $D \rightarrow K_S^0 \pi^+ \pi^-$ vs. $D \rightarrow K_L^0 \pi^0 (\pi^0)$ DT candidates are also reconstructed with the missing-mass squared technique as the K_L^0 particle is not directly detectable in

TABLE II. Summary of ΔE requirements, ST yields (N_{ST}) and ST efficiencies (ϵ_{ST}) for various tags, as well as DT yields (N_{DT}) and DT efficiencies (ϵ_{DT}) for $K_{S,L}^0\pi^+\pi^-$ vs. various tags; where the K_S^0 decay BF is not included in $\epsilon_{\text{DT}}^{K_S^0\pi^+\pi^-}$. The listed uncertainties are statistical only.

Mode	ST			DT			
	ΔE (GeV)	N_{ST}	ϵ_{ST} (%)	$N_{\text{DT}}^{K_S^0\pi^+\pi^-}$	$\epsilon_{\text{DT}}^{K_S^0\pi^+\pi^-}$ (%)	$N_{\text{DT}}^{K_L^0\pi^+\pi^-}$	$\epsilon_{\text{DT}}^{K_L^0\pi^+\pi^-}$ (%)
$K^+\pi^-$	[-0.025, 0.028]	549373 \pm 756	67.28 \pm 0.03	4740 \pm 71	27.28 \pm 0.07	9511 \pm 115	35.48 \pm 0.05
$K^+\pi^-\pi^0$	[-0.044, 0.066]	1076436 \pm 1406	35.12 \pm 0.02	5695 \pm 78	14.45 \pm 0.05	11906 \pm 132	18.21 \pm 0.04
$K^+\pi^-\pi^-\pi^+$	[-0.020, 0.023]	712034 \pm 1705	39.20 \pm 0.02	8899 \pm 95	13.75 \pm 0.05	19225 \pm 176	18.40 \pm 0.04
$K^+e^-\nu_e$		458989 \pm 5724	61.35 \pm 0.02	4123 \pm 75	26.11 \pm 0.07		
<i>CP-even tags</i>							
K^+K^-	[-0.020, 0.021]	57050 \pm 231	63.90 \pm 0.05	443 \pm 22	25.97 \pm 0.07	1289 \pm 41	33.60 \pm 0.07
$\pi^+\pi^-$	[-0.027, 0.030]	20498 \pm 263	68.44 \pm 0.08	184 \pm 14	27.27 \pm 0.07	531 \pm 28	35.60 \pm 0.08
$K_S^0\pi^0\pi^0$	[-0.044, 0.066]	22865 \pm 438	15.81 \pm 0.04	198 \pm 16	6.47 \pm 0.03	612 \pm 35	8.57 \pm 0.03
$\pi^+\pi^-\pi^0$	[-0.051, 0.063]	107293 \pm 716	37.26 \pm 0.04	790 \pm 31	14.28 \pm 0.06	2571 \pm 74	20.29 \pm 0.06
$K_L^0\pi^0$		103787 \pm 7337	48.97 \pm 0.11	913 \pm 41	20.84 \pm 0.04		
<i>CP-odd tags</i>							
$K_S^0\pi^0$	[-0.040, 0.070]	66116 \pm 324	35.98 \pm 0.04	643 \pm 26	14.84 \pm 0.05	861 \pm 46	18.76 \pm 0.06
$K_S^0\eta\gamma\gamma$	[-0.035, 0.038]	9260 \pm 119	30.70 \pm 0.11	89 \pm 10	12.86 \pm 0.05	105 \pm 15	16.78 \pm 0.06
$K_S^0\eta\pi^+\pi^-\pi^0$	[-0.027, 0.032]	2878 \pm 81	16.61 \pm 0.13	23 \pm 5	6.98 \pm 0.03	40 \pm 9	8.88 \pm 0.03
$K_S^0\omega$	[-0.030, 0.039]	24978 \pm 448	16.79 \pm 0.05	245 \pm 17	6.30 \pm 0.03	321 \pm 25	8.14 \pm 0.03
$K_S^0\eta'_{\pi^+\pi^-\eta}$	[-0.028, 0.031]	3208 \pm 88	13.17 \pm 0.09	24 \pm 6	5.06 \pm 0.02	38 \pm 8	6.86 \pm 0.03
$K_S^0\eta'_{\gamma\pi^+\pi^-}$	[-0.026, 0.034]	9301 \pm 139	23.80 \pm 0.10	81 \pm 10	9.87 \pm 0.03	120 \pm 14	12.43 \pm 0.04
$K_L^0\pi^0\pi^0$		50531 \pm 6128	26.20 \pm 0.07	620 \pm 32	11.15 \pm 0.03		
<i>Mixed CP tags</i>							
$K_S^0\pi^+\pi^-$	[-0.022, 0.024]	188912 \pm 756	42.56 \pm 0.03	899 \pm 31	18.53 \pm 0.06	3438 \pm 72	21.61 \pm 0.05
$K_S^0\pi^+\pi^-_{\text{miss}}$				224 \pm 17	5.03 \pm 0.02		
$K_S^0(\pi^0\pi^0_{\text{miss}})\pi^+\pi^-$				710 \pm 34	18.30 \pm 0.04		

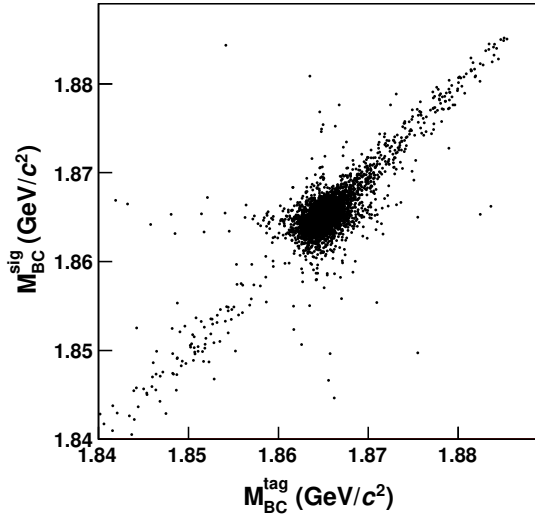


FIG. 3. The two-dimensional M_{BC} distribution. The signal is visible at the center. The concentration of events along the diagonal is from mis-reconstructed DD decays and from $q\bar{q}$ events.

the BESIII detector. In the rest of the event containing a $D \rightarrow K_S^0\pi^+\pi^-$ ST, a further π^0 or $\pi^0\pi^0$ pair is reconstruct-

ed. The event is removed if there are any additional charged tracks in the event. Figures 5(c) and 5(d) show the resultant M_{miss}^2 distributions for $D \rightarrow K_S^0\pi^+\pi^-$ vs. $D \rightarrow K_L^0\pi^0$ and $D \rightarrow K_S^0\pi^+\pi^-$ vs. $D \rightarrow K_L^0\pi^0\pi^0$ candidates, respectively. A peak at the square of the mass of the K_L^0 meson is clearly visible. In this case the peaking backgrounds come from events where the decay products of the K_S^0 have not been reconstructed and therefore the K_S^0 meson has been identified as a K_L^0 meson. The peaking backgrounds from $D \rightarrow K_S^0\pi^0$ and $D \rightarrow K_S^0\pi^0\pi^0$ comprise 5% and 9%, respectively, of the signal sample.

D. Double tags with $K^-e^+\nu_e$

The $D^0 \rightarrow K^-e^+\nu_e$ vs. $\bar{D}^0 \rightarrow K_S^0\pi^+\pi^-$ DT candidates are reconstructed by combining an ST $K_S^0\pi^+\pi^-$ candidate with a K^- and a positron candidate from the remaining tracks in the event. Events with more than two additional charged tracks that have not been used in the ST selection are vetoed. Information concerning the undetected neutrino is obtained through the kinematic variable

$$U_{\text{miss}} \equiv (\sqrt{s}/2 - E_K - E_e) - |\vec{p}_{\text{miss}}|, \quad (14)$$

where E_K and E_e are the energy of the kaon and electron from the semi-leptonic D decay candidate, and \vec{p}_{miss} is the missing momentum carried by the neutrino. The momentum

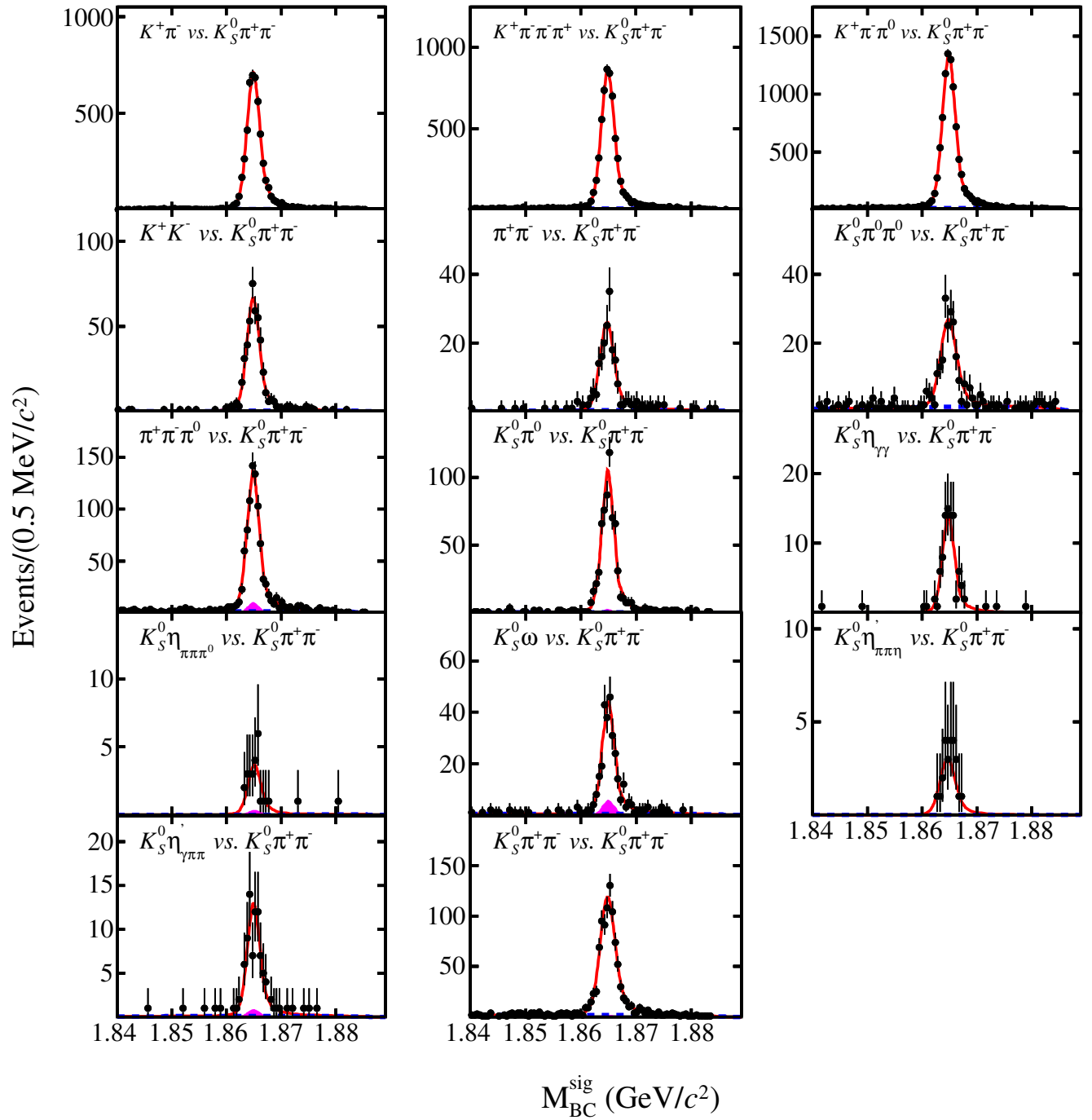


FIG. 4. The projections of the two-dimensional fits of $D^0 \rightarrow K_S^0 \pi^+ \pi^-$ vs. various ST on the M_{BC}^{sig} distribution. The black points represent the data. Overlaid is the fit projection in the continuous red line. The blue dashed line indicates the combinatorial component and the peaking background contribution is shown by the shaded areas (pink)

\vec{p}_{miss} is defined as $\vec{p}_{\text{miss}} = \vec{p}_{\text{sig}} - \vec{p}_K - \vec{p}_e$. Figure 5(e) shows the U_{miss} distribution for $D^0 \rightarrow K^- e^+ \nu_e$ candidates in data, where a peak centered on $U_{\text{miss}} = 0$ is observed due to the negligible mass of the neutrino.

E. Double tags with $K_L^0 \pi^+ \pi^-$

To identify the signal candidates from $D \rightarrow K_L^0 \pi^+ \pi^-$ decays, only two additional and oppositely charged good tracks

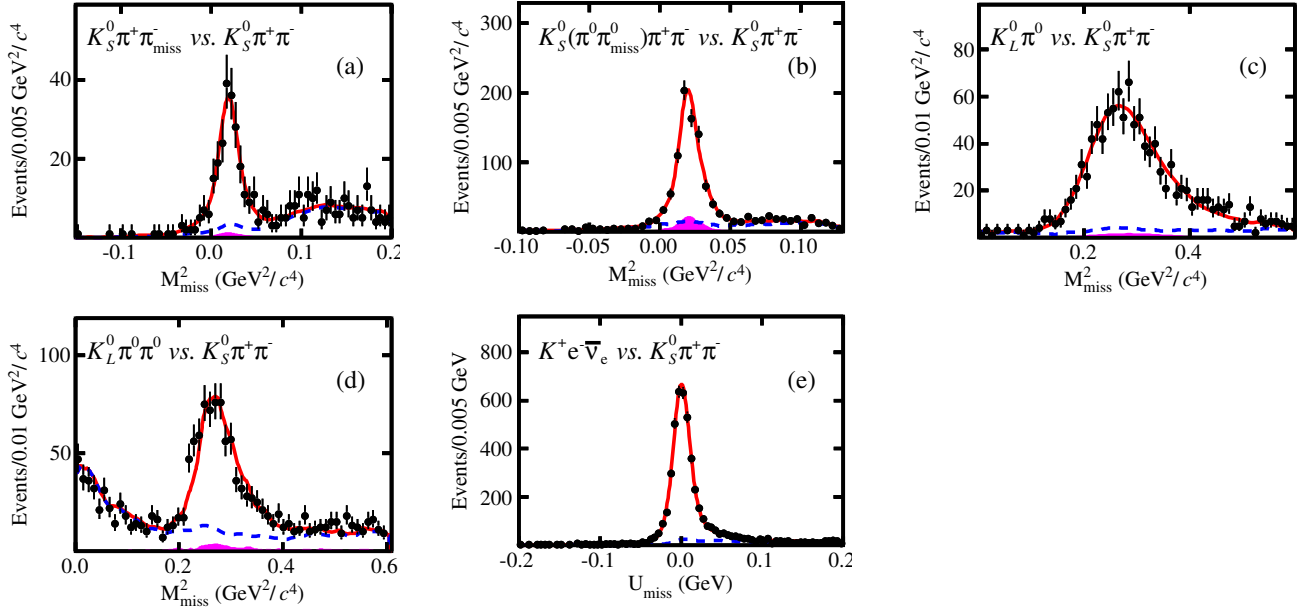


FIG. 5. Fits to M_{miss}^2 or U_{miss} distributions for the candidates of $D^0 \rightarrow K_S^0 \pi^+ \pi^-$ vs. various tags in data. Points with error bars represent data, the blue dashed curves are the fitted combinatorial backgrounds, the shaded areas (pink) show the MC-simulated peaking backgrounds, and the red solid curves show the total fits.

are required in an event where one of the ST has been selected. These two tracks are identified as the π^+ and π^- from the D meson. Events that contain any additional charged tracks with the distance of closest approach to the IP less than 20 cm along the beam direction are vetoed. This requirement reduces background from $K_S^0 \rightarrow \pi^+ \pi^-$ decays. To reject the backgrounds containing π^0 and η mesons, events are vetoed where the invariant mass of any further photon pairs are within the ranges $(0.098, 0.165)$ GeV/c^2 and $(0.48, 0.58)$ GeV/c^2 . This requirement retains about 80% of the signal while reducing more than 90% of the peaking backgrounds from $D \rightarrow K_S^0 \pi^+ \pi^-$, where $K_S^0 \rightarrow \pi^0 \pi^0$. The residual peaking background rate in $D \rightarrow K_L^0 \pi^+ \pi^-$ selected candidates is 5% of the signal yield and is primarily from the decay $D \rightarrow K_S^0(\pi^0 \pi^0) \pi^+ \pi^-$. Figure 6 shows the M_{miss}^2 distributions of the accepted $D \rightarrow K_L^0 \pi^+ \pi^-$ candidates in data.

F. Dalitz plot distributions

The DT yields of $K_S^0 \pi^+ \pi^-$ and $K_L^0 \pi^+ \pi^-$ tagged by different channels are shown in the fifth and seventh columns of Table II, respectively. Their selection efficiencies (ϵ^{DT}) are also listed in the sixth and eighth columns of Table II. The DT selection efficiencies are determined in simulation where the signal and tag D meson are both forced to decay to the final states in which they are reconstructed. The efficiency is determined as the number of DT candidates selected divided by the number of events generated.

The DT yields of $D \rightarrow K_{S(L)}^0 \pi^+ \pi^-$ involving a CP eigenstate are a factor of 5.3(9.2) larger than those report-

ed in Ref. [23]. The yields of $K_S^0 \pi^+ \pi^-$ tagged with $D \rightarrow K_{S(L)}^0 \pi^+ \pi^-$ decays are a factor of 3.9(3.0) larger than those in Ref. [23]. These increases come not only from the larger data set available at BESIII but also from the additional tag decay modes and partial reconstruction selection techniques.

The resolutions of $M_{K_S^0 \pi^\pm}^2$ and $M_{K_L^0 \pi^\pm}^2$ on the Dalitz plot are improved by requiring that the two neutral D mesons conserve energy and momentum in the center-of-mass frame, and the decay products from each D meson are constrained to the nominal D^0 mass [33]. In addition the K_S^0 decay products are constrained to the K_S^0 nominal mass [33]. Finally, the missing mass of K_L^0 candidates is constrained to the nominal value [33]. The study of simulated data indicates that the resulting resolutions of $M_{K_S^0 \pi^\pm}^2$ and $M_{K_L^0 \pi^\pm}^2$ are 0.0068 GeV^2/c^4 and 0.0105 GeV^2/c^4 for $D \rightarrow K_S^0 \pi^+ \pi^-$ and $D \rightarrow K_L^0 \pi^+ \pi^-$, respectively. It should be noted that the finite detector resolution can cause the selected events to migrate between Dalitz plot bins after reconstruction, which should be incorporated in evaluating the expected DT candidates observed in Dalitz plot bins. More details are presented in Secs. VB and VC.

The Dalitz plots for $D^0 \rightarrow K_S^0 \pi^+ \pi^-$ and $D^0 \rightarrow K_L^0 \pi^+ \pi^-$ vs. the flavor tags selected from the data are shown in Fig. 7. In order to merge the D^0 and \bar{D}^0 decays the exchange of coordinates $M_{K_{S,L}^0 \pi^\pm}^2 \leftrightarrow M_{K_{S,L}^0 \pi^\mp}^2$ is performed for the \bar{D}^0 decays. Figure 7 also shows the CP -even and CP -odd tagged signal channels selected in the data. The effect of the quantum correlation in the data is immediately obvious by studying the differences in these plots. Most noticeably, the CP -odd component $D \rightarrow K_S^0 \rho^0$ is visible in the $D \rightarrow K_S^0 \pi^+ \pi^-$ decay

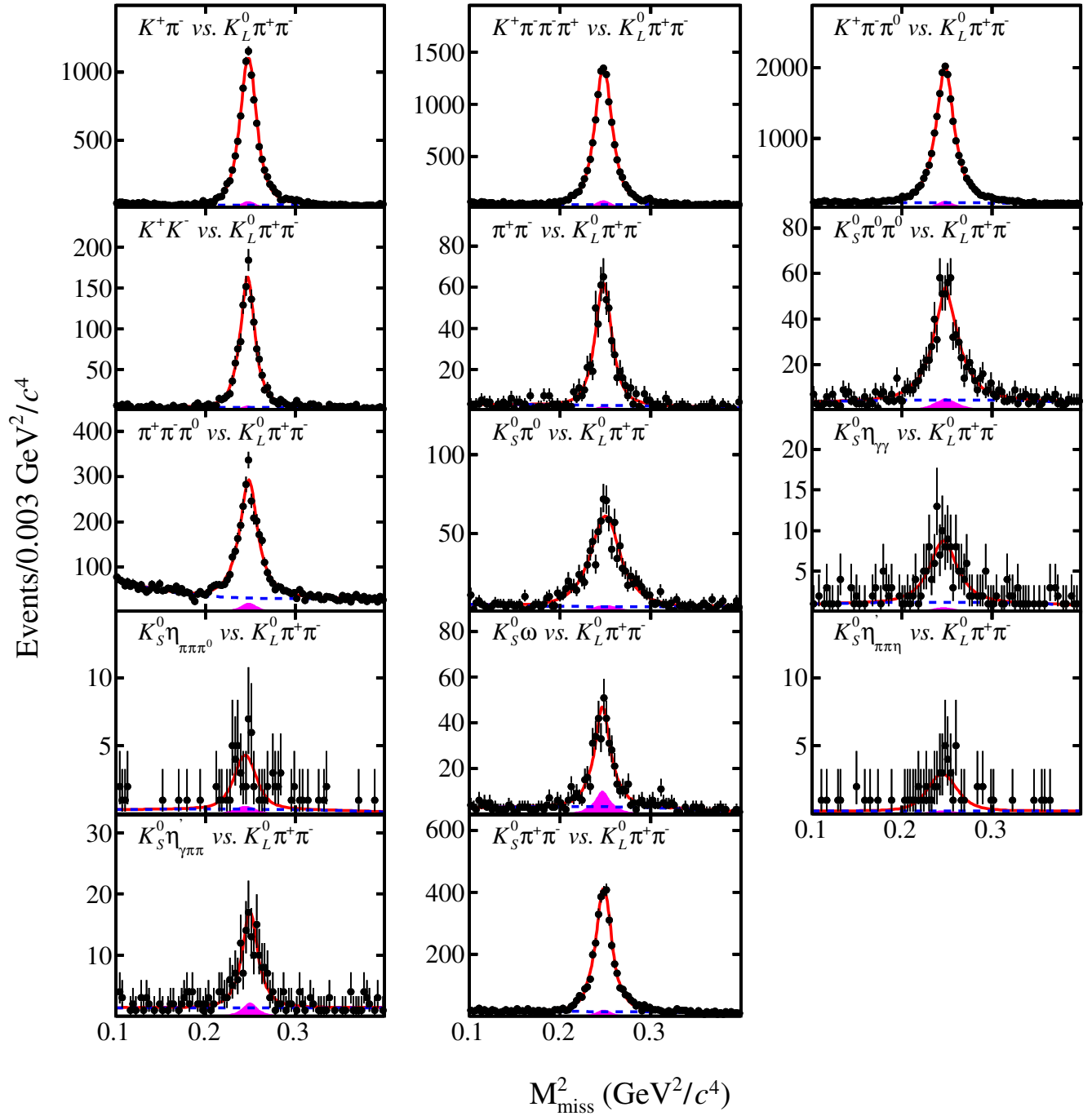


FIG. 6. Fits to M_{miss}^2 distributions for the candidates of $D^0 \rightarrow K_L^0 \pi^+ \pi^-$ vs. various tags in data. Points with error bars are data, the blue dashed curves are the fitted combinatorial backgrounds, the shaded areas (pink) show the MC-simulated peaking backgrounds, and the red solid curves are the total fits.

when tagged by CP -even decays, but is absent when tagged by CP -odd decays.

V. DETERMINATION OF $c_i^{(\prime)}$ AND $s_i^{(\prime)}$

A. Double-tag yields in Dalitz plot bins

The fit used to determine the strong-phase parameters is based on the Poisson probability to observe N events in a

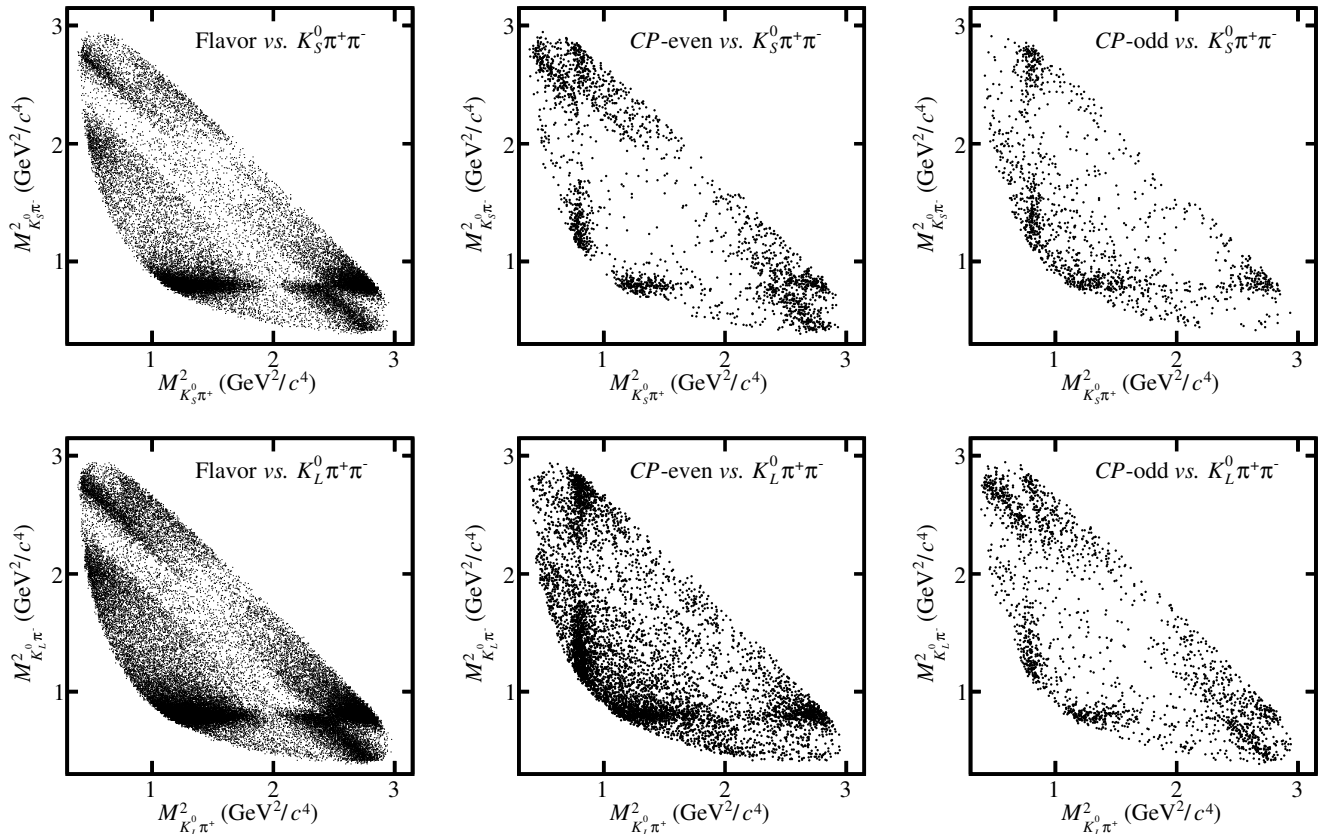


FIG. 7. Dalitz plots of $K_S^0 \pi^+ \pi^-$ and $K_L^0 \pi^+ \pi^-$ events in data.

phase space region given the expectation value $\langle N \rangle$. To measure the observed yields, the data are divided into the phase space regions based on their Dalitz plot coordinates (m_+^2 , m_-^2). A small fraction of candidates ($\sim 0.3\%$) fall outside the defined bins. This is because the knowledge of the D^0 mass has improved since the model used to define the phase space regions was determined. This improvement leads to a slightly larger allowed phase space in the current analysis compared to the maps of the phase space regions. These outlying candidates are assigned to the bins to which they are closest.

In the $K_{S,L}^0 \pi^+ \pi^-$ Dalitz plots of the flavor-tagged samples, the positive and negative bins are distinguishable, and hence yields are measured in 16 bins for each final state. In contrast, the CP -tagged Dalitz plots are symmetric about the line $m_+^2 = m_-^2$ (see Eqs. (7) and (10)) and so the entries are summed for bins i and $-i$. Exploiting this symmetry reduces the statistical fluctuations for those CP tags where the yields are low.

The $K_{S(L)}^0 \pi^+ \pi^-$ vs. $K_S^0 \pi^+ \pi^-$ samples are described by two Dalitz plots. Therefore it is necessary to determine the yields for the i th bin (\mathcal{D}_i) of one plot and the j th bin (\mathcal{D}_j) of the other, in order to obtain the quantities M_{ij} (M'_{ij}) that occur in Eq. (9) [Eq. (11)]. Considering each half of both plots gives the possibilities $M_{ij}^{(i)}$, $M_{i-j}^{(i)}$, $M_{-ij}^{(i)}$ and $M_{-i-j}^{(i)}$, which

obey the following relations:

$$M_{ij}^{(i)} = M_{-i-j}^{(i)}, \quad M_{-ij}^{(i)} = M_{i-j}^{(i)}, \quad \text{and} \quad M_{ij}^{(i)} = M_{i-j}^{(i)}. \quad (15)$$

It follows that events can be classified into those where both decays occur in the Dalitz plots on the same side of the $m_+^2 = m_-^2$ line, and those when they are on different sides. For the case where both D mesons are fully reconstructed as $D \rightarrow K_S^0 \pi^+ \pi^-$, it is not possible to distinguish between \mathcal{D}_i and \mathcal{D}_j , and thus M_{ij} is combined with M_{ji} . The partially reconstructed $D \rightarrow K_S^0 \pi^+ \pi^-$ samples are treated in the same way, despite the distinguishability of the final states, in order to avoid low yields. In the $K_L^0 \pi^+ \pi^-$ vs. $K_S^0 \pi^+ \pi^-$ sample \mathcal{D}_i is chosen to specify the $K_S^0 \pi^+ \pi^-$ Dalitz plot bin, and \mathcal{D}_j the $K_L^0 \pi^+ \pi^-$ bin. In this case M'_{ij} and M'_{ji} are distinguishable and cannot be combined. Following these considerations, the samples with two Dalitz plots are divided into 72 and 128 bins.

In each bin of phase space there are candidates that are from signal, combinatorial background, and peaking backgrounds. The yields for each DT mode are determined in the same way as in Sec. IV, although in some regions where the yields are low it is necessary to fix some parameters from the fit to data over the full phase space. The observed combinatorial background yield is determined in the fit and not considered further. Although the expected peaking-background yield can

be calculated with MC simulation, the fit cannot distinguish the observed peaking background yield from the signal yield. Therefore the observed yield N^{obs} in each phase space region is the sum of signal and peaking background.

B. Determination of K_i and K'_i

The yields of K_i and K'_i are necessary to determine the expected yields in the decays sensitive to the strong-phase parameters. As discussed in Sec. IV F, the finite detector resolution can cause the individual decays to migrate between Dalitz plot bins after reconstruction. Furthermore, the migration effects between $D^0 \rightarrow K_S^0 \pi^+ \pi^-$ and $D^0 \rightarrow K_L^0 \pi^+ \pi^-$ are also different due to their resolution differences. Studies indicate that neglecting bin migration induces average biases of 0.7 (0.3) times the statistical uncertainty in the determination of c_i (s_i), and hence it is important to correct for this effect in the analysis.

To account for this effect, the number of observed signal events ($N_i^{\text{obs}(\prime)}$) for flavor-tagged $K_{S(L)}^0 \pi^+ \pi^-$ decays in the i th bin of the Dalitz plot is written

$$N_i^{\text{obs}(\prime)} = \sum_{j=1}^{N_{\text{bins}}} \epsilon_{ij} K_j^{(\prime)}, \quad (16)$$

where ϵ_{ij} is the efficiency matrix which describes the reconstruction efficiency and migration effects across Dalitz plot bins associated with reconstruction of tag and signal decays. The efficiency matrix ϵ_{ij} can be obtained by analyzing a sample of signal MC events which are generated as $e^+ e^- \rightarrow \psi(3770) \rightarrow D^0 \bar{D}^0$, where the \bar{D}^0 meson decays to the ST modes and $D^0 \rightarrow K_{S(L)}^0 \pi^+ \pi^-$. The efficiency ma-

trix ϵ_{ij} for detecting $D \rightarrow K_{S(L)}^0 \pi^+ \pi^-$ decay is given by

$$\epsilon_{ij} = \frac{N_{ij}^{\text{rec}}}{N_j^{\text{gen}}} \times \frac{1}{\epsilon_{\text{ST}}}, \quad (17)$$

where N_{ij}^{rec} is the number of signal MC events generated in the j th Dalitz plot bin and reconstructed in the i th Dalitz plot bin, N_j^{gen} is the number of signal MC events which are generated in the j th Dalitz plot bin and ϵ_{ST} is the ST efficiency. An example of the efficiency matrix ϵ_{ij} for $K_{S(L)}^0 \pi^+ \pi^-$ vs. $K^+ \pi^-$ in the equal $\Delta\delta_D$ binning scheme is shown in Table III. Thus, the value of $K_i^{(\prime)}$ in the i th Dalitz plot bin for $D^0 \rightarrow K_{S(L)}^0 \pi^+ \pi^-$ decay is obtained by

$$K_i^{(\prime)} = \sum_{j=1}^{N_{\text{bins}}} (\epsilon^{-1})_{ij} N_j^{\text{obs}(\prime)}. \quad (18)$$

In addition, the migration effects in the i th Dalitz plot bin can be estimated by using $R_i = \epsilon_{ii} / \sum_j \epsilon_{ij}$, which denotes the fraction of the reconstructed events falling outside the true Dalitz plot bins. From the efficiency matrix ϵ_{ij} listed in Table III, it is estimated that the bin migration effects range within (3-12)% and (3-18)% for the $K_S^0 \pi^+ \pi^-$ and $K_L^0 \pi^+ \pi^-$ signals with the equal $\Delta\delta_D$ binning scheme, respectively.

Moreover, the event yields of $K_S^0 \pi^+ \pi^-$ and $K_L^0 \pi^+ \pi^-$ selected against hadronic flavored tags are also contaminated by DCS decays [22, 23]. To account for this effect, the flavor-tagged yield in each Dalitz plot bin is scaled by a correction factor $f_i^{(\prime)}$ (f_i for $K_S^0 \pi^+ \pi^-$ and f'_i for $K_L^0 \pi^+ \pi^-$). The correction factors for the hadronic tags $K^+ \pi^-$, $K^+ \pi^- \pi^0$ and $K^+ \pi^- \pi^- \pi^+$ are calculated by

$$f_i = \frac{\int_i |f(m_+^2, m_-^2)|^2 dm_+^2 dm_-^2}{\int_i (|f(m_+^2, m_-^2)|^2 + (r_D^F)^2 |f(m_-^2, m_+^2)|^2 - 2r_D^F R_F \mathcal{R}[e^{i\delta_D^F} f(m_+^2, m_-^2) f^*(m_-^2, m_+^2)]) dm_+^2 m_-^2},$$

$$f'_i = \frac{\int_i |f'(m_+^2, m_-^2)|^2 dm_+^2 dm_-^2}{\int_i (|f'(m_+^2, m_-^2)|^2 + (r_D^F)^2 |f'(m_-^2, m_+^2)|^2 + 2r_D^F R_F \mathcal{R}[e^{i\delta_D^F} f'(m_+^2, m_-^2) f'^*(m_-^2, m_+^2)]) dm_+^2 m_-^2}. \quad (19)$$

Here r_D^F is the ratio of the DCS amplitude to the Cabibbo-favored decay amplitude and δ_D^F is the corresponding strong-phase difference. For multibody final states these two quantities are averaged over the decay phase space. The coherence factor [38] R_F equals unity for two-body decays, and has been measured for $D \rightarrow K^+ \pi^- \pi^- \pi^+$ and $D \rightarrow K^+ \pi^- \pi^0$ [39, 40]. The values of these parameters and the corresponding references are given in Table IV. Furthermore, $f(m_+^2, m_-^2)$ and $f'(m_+^2, m_-^2)$ are the amplitudes of $D^0 \rightarrow K_S^0 \pi^+ \pi^-$ and $D^0 \rightarrow K_L^0 \pi^+ \pi^-$, respectively. The amplitude of the decay $D^0 \rightarrow K_S^0 \pi^+ \pi^-$ is taken from the model given in Ref. [42]. The decay amplitude of $D^0 \rightarrow K_L^0 \pi^+ \pi^-$ has not been studied, however a decay model can be estimated by adjusting the $D^0 \rightarrow K_S^0 \pi^+ \pi^-$ model in the same way as dis-

cussed in Refs. [22, 23], and using that K_S^0 and K_L^0 mesons are of opposite CP , to an excellent approximation. Starting with the $D^0 \rightarrow K_S^0 \pi^+ \pi^-$ model in Ref. [42], the Cabibbo-favored amplitudes are unchanged and the amplitudes of the DCS components gain a factor -1 . For the CP -eigenstate amplitudes, such as $K_S^0 \rho(770)^0$, the $D^0 \rightarrow K_L^0 \pi^+ \pi^-$ amplitude can be related to the $D^0 \rightarrow K_S^0 \pi^+ \pi^-$ amplitude by multiplying the latter by a factor $(1 - 2re^{i\delta})$ [43], where r is of the order of $\tan^2 \theta_C$. Here, θ_C is the Cabibbo angle and δ is an unknown phase. To determine central values for f'_i , the parameters r and δ are varied a number of times where δ is assumed to have an equal probability to lie between 0° and 360° and r is assumed to have a Gaussian distribution with mean $\tan^2 \theta_C$ and width $0.5 \times \tan^2 \theta_C$. The mean value of

TABLE III. Efficiency matrix ϵ_{ij} (%) for $K_{S,L}^0\pi^+\pi^-$ vs. $K^+\pi^-$ in the equal $\Delta\delta_D$ binning scheme. The column gives the true bins j , while the row gives the reconstructed bin i , in which the decay BF of $K_S^0 \rightarrow \pi^+\pi^-$ is not included.

Bins(True) (Rec)	1	-1	2	-2	3	-3	4	-4	5	-5	6	-6	7	-7	8	-8
ϵ_{ij} for $K_S^0\pi^+\pi^-$ vs. $K^+\pi^-$																
1	36.53	0.24	2.40	0.00	0.20	0.04	0.11	0.07	0.05	0.01	0.11	0.04	0.20	0.00	2.28	0.02
-1	0.12	38.84	0.01	1.63	0.01	0.24	0.04	0.07	0.01	0.07	0.01	0.10	0.01	0.17	0.01	1.74
2	1.33	0.00	38.05	0.00	1.33	0.01	0.02	0.00	0.00	0.00	0.01	0.00	0.06	0.00	0.14	0.00
-2	0.00	0.36	0.01	39.12	0.01	0.63	0.01	0.08	0.00	0.00	0.00	0.03	0.01	0.04	0.00	0.03
3	0.11	0.01	1.21	0.01	41.05	0.10	1.34	0.04	0.01	0.01	0.03	0.01	0.04	0.01	0.08	0.02
-3	0.02	0.04	0.02	0.49	0.05	41.59	0.04	0.84	0.00	0.01	0.04	0.05	0.04	0.06	0.04	0.01
4	0.03	0.01	0.06	0.01	0.53	0.01	40.59	0.03	0.26	0.01	0.02	0.01	0.03	0.01	0.03	0.02
-4	0.03	0.02	0.04	0.04	0.07	0.96	0.03	42.10	0.00	0.33	0.01	0.06	0.04	0.08	0.01	0.02
5	0.04	0.01	0.02	0.00	0.05	0.04	0.90	0.01	38.14	0.00	1.16	0.00	0.03	0.00	0.02	0.01
-5	0.03	0.06	0.04	0.02	0.05	0.05	0.02	0.93	0.00	38.66	0.00	1.77	0.02	0.08	0.01	0.03
6	0.06	0.00	0.04	0.00	0.06	0.00	0.05	0.02	0.80	0.00	35.50	0.03	0.97	0.00	0.08	0.00
-6	0.01	0.02	0.02	0.01	0.03	0.03	0.02	0.02	0.00	0.64	0.00	37.54	0.01	1.93	0.01	0.07
7	0.17	0.01	0.14	0.00	0.09	0.04	0.03	0.04	0.04	0.00	1.93	0.03	35.50	0.01	2.17	0.00
-7	0.01	0.07	0.03	0.06	0.04	0.07	0.06	0.07	0.01	0.02	0.00	1.39	0.01	36.86	0.01	0.79
8	2.00	0.00	0.25	0.00	0.12	0.03	0.03	0.03	0.02	0.00	0.13	0.02	1.99	0.03	35.24	0.00
-8	0.01	0.72	0.03	0.10	0.03	0.05	0.01	0.01	0.00	0.03	0.01	0.07	0.01	1.81	0.01	37.94
ϵ_{ij} for $K_L^0\pi^+\pi^-$ vs. $K^+\pi^-$																
1	45.66	0.61	4.14	0.00	0.20	0.00	0.07	0.00	0.06	0.00	0.37	0.00	0.58	0.00	4.62	0.01
-1	0.36	51.88	0.00	2.96	0.00	0.20	0.00	0.13	0.00	0.08	0.01	0.13	0.02	0.49	0.02	3.32
2	2.25	0.00	46.88	0.00	1.83	0.00	0.11	0.00	0.00	0.00	0.03	0.00	0.10	0.00	0.30	0.00
-2	0.00	0.68	0.00	50.04	0.00	1.04	0.00	0.06	0.00	0.01	0.00	0.06	0.00	0.08	0.00	0.14
3	0.12	0.00	1.66	0.00	50.44	0.00	2.10	0.00	0.03	0.00	0.08	0.00	0.02	0.00	0.05	0.00
-3	0.00	0.06	0.00	0.62	0.00	52.50	0.00	1.30	0.00	0.01	0.00	0.05	0.00	0.06	0.00	0.03
4	0.02	0.00	0.03	0.00	0.74	0.00	51.02	0.00	0.47	0.00	0.04	0.00	0.01	0.00	0.01	0.00
-4	0.00	0.01	0.00	0.04	0.00	1.35	0.00	51.33	0.00	0.50	0.00	0.08	0.00	0.01	0.00	0.00
5	0.04	0.00	0.02	0.00	0.04	0.00	1.41	0.00	51.23	0.00	1.98	0.00	0.06	0.00	0.04	0.00
-5	0.00	0.09	0.00	0.01	0.00	0.07	0.00	1.50	0.00	50.45	0.00	3.01	0.00	0.18	0.00	0.07
6	0.11	0.00	0.04	0.00	0.03	0.00	0.11	0.00	1.24	0.00	45.69	0.00	1.70	0.00	0.12	0.00
-6	0.00	0.07	0.00	0.01	0.00	0.05	0.00	0.08	0.00	0.99	0.00	47.92	0.00	3.10	0.00	0.12
7	0.31	0.00	0.19	0.00	0.10	0.00	0.08	0.00	0.07	0.00	3.52	0.00	44.30	0.00	3.92	0.00
-7	0.00	0.09	0.00	0.10	0.00	0.09	0.00	0.04	0.00	0.04	0.00	2.23	0.00	45.24	0.00	1.47
8	3.53	0.01	0.44	0.00	0.12	0.00	0.04	0.00	0.03	0.00	0.36	0.00	4.01	0.00	42.92	0.00
-8	0.01	1.35	0.00	0.32	0.00	0.09	0.00	0.02	0.00	0.02	0.00	0.19	0.00	3.04	0.00	49.95

the resulting distribution of f'_i is taken as the nominal value of that parameter.

The event fraction $F_i^{(\prime)}$, defined as $F_i^{(\prime)} = K_i^{(\prime)}/A_D$, where $A_D = \sum_{i=1}^8 (K_i^{(\prime)} + K_{-i}^{(\prime)})$, is computed for each flavor-tag.

Figure 8 shows the measured values of F_i and F'_i in various Dalitz plot bins for the flavor-tagged $D^0 \rightarrow K_S^0\pi^+\pi^-$ and $D^0 \rightarrow K_L^0\pi^+\pi^-$ events, respectively, observed in data. The measured values of F_i and F'_i are consistent between the different categories of flavor tags, which provides a good validation for the extracted K_i and K'_i in data. In order to recover the summed K_i from all flavor-tagged $K_S^0\pi^+\pi^-$ with $K_S^0 \rightarrow \pi^+\pi^-$ used in this analysis, the values of F_i in Table V should be multiplied by 58607, 58647, and 58595 for the equal $\Delta\delta_D$, optimal, and modified binning schemes, respectively. To obtain the values of K'_i the corresponding factors are 80718, 80661, and 80706.

TABLE IV. Values of the parameters used to make the corrections to the flavor-tagged yields.

F	r_D^F (%)	δ_D^F ($^\circ$)	R_F
$K\pi\pi\pi$	5.49 ± 0.06 [39, 40]	128^{+28}_{-17} [39, 40]	$0.43^{+0.17}_{-0.13}$ [39, 40]
$K\pi\pi^0$	4.47 ± 0.12 [39, 40]	198^{+14}_{-15} [39, 40]	0.81 ± 0.06 [39, 40]
$K\pi$	5.86 ± 0.02 [41]	$194.7^{+8.4}_{-17.6}$ [41]	1

C. Expected DT yields in Dalitz plot bins

The expected yields, $\langle N \rangle$, are a sum of expected signal and peaking background contributions. The expected signal yields are calculated from the equations given in Sec. II, with adjustments made to account for bin migration and selection and reconstruction efficiencies, so that they can be compared to

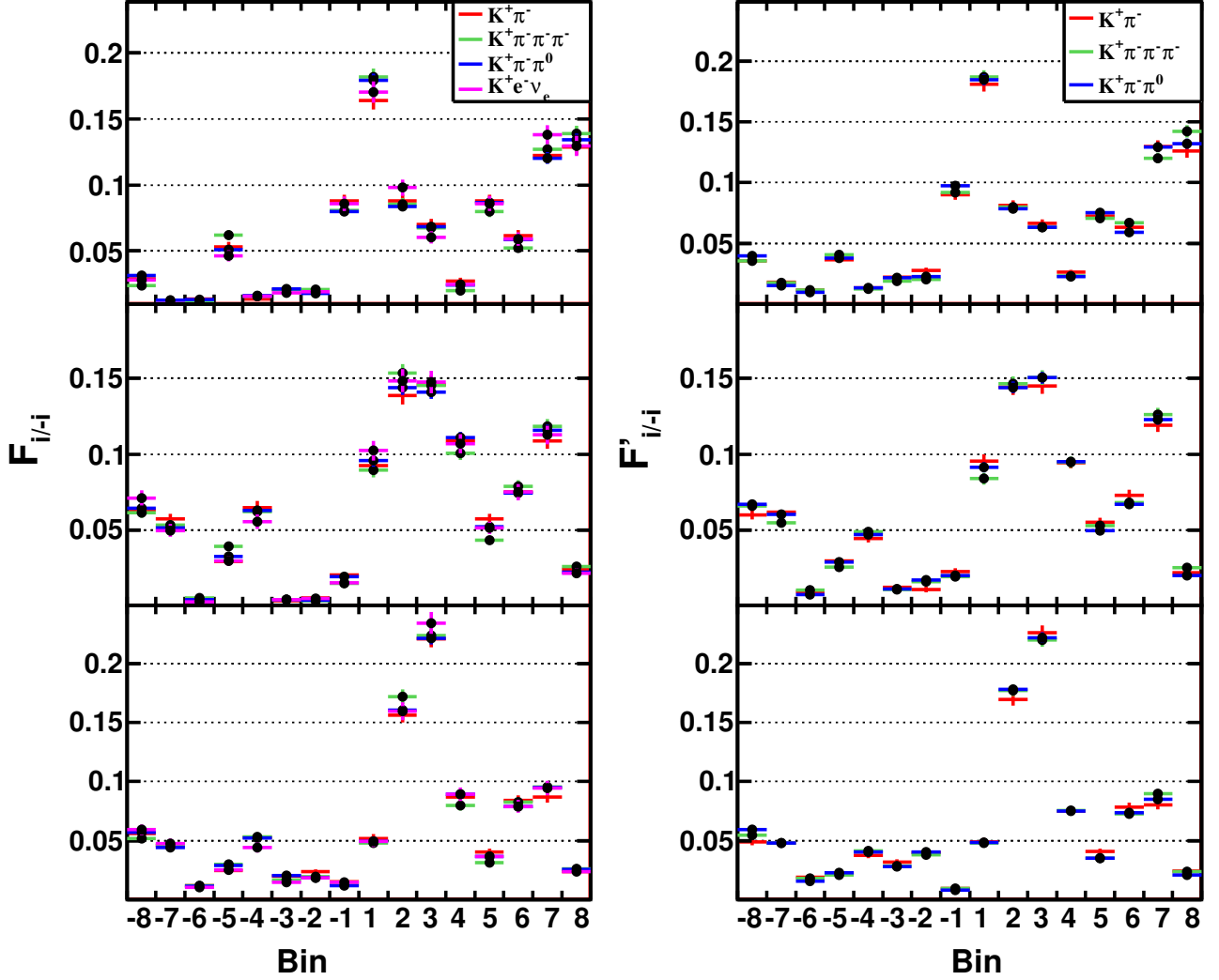


FIG. 8. Event fractions in Dalitz plot bins in data; (left) $F_{i/-i}$ for $K_S^0\pi^+\pi^-$ and (right) $F'_{i/-i}$ for $K_L^0\pi^+\pi^-$ from (top) equal $\Delta\delta_D$, (middle) optimal and (bottom) modified optimal binning schemes, respectively. The horizontal and vertical error bars denote the bin intervals and the statistical uncertainties of the event fractions, respectively.

the yields from data. For CP -tagged $D \rightarrow K_S^0\pi^+\pi^-$ decays, the expected signal yield in the i th bin is given by

$$M_i = h_{CP} \sum_j^8 \epsilon_{ij}^{K_S^0\pi^+\pi^-} \times [K_j - (2F_{CP} - 1)2c_j\sqrt{K_j K_{-j}} + K_{-j}], \quad (20)$$

where $\epsilon_{ij}^{K_S^0\pi^+\pi^-}$ is the efficiency matrix for detecting $D \rightarrow K_S^0\pi^+\pi^-$ vs. the particular CP tag under consideration defined similarly as in Eq. (17). The efficiency matrix is defined to take into account the merging of the i th and $-i$ th regions in data (*i.e.* it has size 8×8). The normalization factor h_{CP} is defined as S_{CP}/S_{FT} . For CP -tagged $D \rightarrow K_L^0\pi^+\pi^-$, the

expected signal yield in the i th bin is given by

$$M'_i = h'_{CP} \sum_j^8 \epsilon_{ij}^{K_L^0\pi^+\pi^-} \times [K'_j - (2F_{CP} - 1)2c'_j\sqrt{K'_j K'_{-j}} + K'_{-j}], \quad (21)$$

where h'_{CP} is given by $S_{CP}/S_{FT'}$, and $S_{FT'}$ is the sum of ST yields for the three hadronic flavor tags used to determine the values of K'_i .

For the DT $D \rightarrow K_S^0\pi^+\pi^-$ vs. $D \rightarrow K_S^0\pi^+\pi^-$ the efficiency matrix, $\epsilon_{nm}^{K_S^0\pi^+\pi^- \text{ vs. } K_S^0\pi^+\pi^-}$, is a 72×72 matrix where each value of the indices n and m corresponds to one of the 72 distinct bin-pairs. The expected signal yields are expressed

TABLE V. The values of F_i and F'_i using all flavor-tagged DT samples, for each of the three binning schemes. The uncertainties are statistical only.

Bin	Equal $\Delta\delta_D$ binning		Optimal binning		Modified optimal binning	
	F_i	F'_i	F_i	F'_i	F_i	F'_i
1	0.176 ± 0.003	0.184 ± 0.003	0.095 ± 0.002	0.090 ± 0.002	0.049 ± 0.002	0.048 ± 0.002
-1	0.083 ± 0.002	0.094 ± 0.002	0.018 ± 0.001	0.021 ± 0.001	0.013 ± 0.001	0.009 ± 0.001
2	0.087 ± 0.002	0.079 ± 0.002	0.146 ± 0.003	0.145 ± 0.003	0.162 ± 0.003	0.176 ± 0.003
-2	0.019 ± 0.001	0.023 ± 0.001	0.004 ± 0.001	0.015 ± 0.001	0.020 ± 0.001	0.040 ± 0.001
3	0.067 ± 0.002	0.064 ± 0.002	0.144 ± 0.003	0.149 ± 0.003	0.224 ± 0.003	0.222 ± 0.003
-3	0.021 ± 0.001	0.021 ± 0.001	0.004 ± 0.001	0.011 ± 0.001	0.018 ± 0.001	0.029 ± 0.001
4	0.024 ± 0.001	0.023 ± 0.001	0.107 ± 0.002	0.095 ± 0.002	0.086 ± 0.002	0.075 ± 0.002
-4	0.016 ± 0.001	0.013 ± 0.001	0.062 ± 0.002	0.047 ± 0.001	0.051 ± 0.002	0.040 ± 0.001
5	0.085 ± 0.002	0.073 ± 0.002	0.051 ± 0.002	0.052 ± 0.002	0.036 ± 0.001	0.036 ± 0.001
-5	0.053 ± 0.002	0.038 ± 0.001	0.033 ± 0.001	0.028 ± 0.001	0.028 ± 0.001	0.022 ± 0.001
6	0.058 ± 0.002	0.062 ± 0.002	0.076 ± 0.002	0.069 ± 0.002	0.081 ± 0.002	0.074 ± 0.002
-6	0.012 ± 0.001	0.010 ± 0.001	0.004 ± 0.001	0.009 ± 0.001	0.011 ± 0.001	0.017 ± 0.001
7	0.125 ± 0.003	0.126 ± 0.002	0.114 ± 0.002	0.123 ± 0.002	0.093 ± 0.002	0.085 ± 0.002
-7	0.012 ± 0.001	0.016 ± 0.001	0.053 ± 0.002	0.059 ± 0.002	0.045 ± 0.002	0.048 ± 0.002
8	0.134 ± 0.003	0.134 ± 0.003	0.024 ± 0.001	0.022 ± 0.001	0.025 ± 0.001	0.022 ± 0.001
-8	0.028 ± 0.001	0.037 ± 0.001	0.065 ± 0.002	0.065 ± 0.002	0.056 ± 0.002	0.055 ± 0.001

as

$$M_n = h_{\text{corr}} \sum_{m=1}^{m=72} \epsilon_{nm}^{K_S^0 \pi^+ \pi^- \text{ vs. } K_S^0 \pi^+ \pi^-} [K_{i_m} K_{-j_m} + K_{-i_m} K_{j_m} - 2\sqrt{K_{i_m} K_{-j_m} K_{-i_m} K_{j_m}} (c_{i_m} c_{j_m} + s_{i_m} s_{j_m})], \quad (22)$$

where i_m and j_m correspond to the i th and j th bins of the m th bin-pair and $h_{\text{corr}} = (N_{DD}/S_{\text{FT}}^2) \times \alpha\beta$. The constant α results from the symmetry relations used to combine bin pairs. The value of α is 1 when the i, j values of the index n satisfy $|i| = |j|$ and 2 otherwise. The constant β arises from the symmetry of the signal and tag decays and has value 1 for the selections where both K_S^0 mesons decay via $K_S^0 \rightarrow \pi^+ \pi^-$, and value $2 \times \mathcal{B}(K_S^0 \rightarrow \pi^0 \pi^0)/\mathcal{B}(K_S^0 \rightarrow \pi^+ \pi^-)$ when one K_S^0 meson decays to the $\pi^0 \pi^0$ final state. Here, $\mathcal{B}(K_S^0 \rightarrow \pi^0 \pi^0)$ and $\mathcal{B}(K_S^0 \rightarrow \pi^+ \pi^-)$ are BFs for $K_S^0 \rightarrow \pi^0 \pi^0$ and $K_S^0 \rightarrow \pi^+ \pi^-$, respectively. For the DT $D \rightarrow K_L^0 \pi^+ \pi^-$ vs. $D \rightarrow K_S^0 \pi^+ \pi^-$ the expected signal yields are expressed as

$$M'_n = h'_{\text{corr}} \sum_{m=1}^{m=128} \epsilon_{nm}^{K_L^0 \pi^+ \pi^- \text{ vs. } K_S^0 \pi^+ \pi^-} [K_{i_m} K'_{-j_m} + K_{-i_m} K'_{j_m} - 2\sqrt{K_{i_m} K'_{-j_m} K_{-i_m} K'_{j_m}} (c_{i_m} c'_{j_m} + s_{i_m} s'_{j_m})], \quad (23)$$

where $h'_{\text{corr}} = 2N_{DD}/(S_{\text{FT}}' S_{\text{FT}})$. The DT efficiency matrix of detecting $D \rightarrow K_L^0 \pi^+ \pi^-$ vs. $D \rightarrow K_S^0 \pi^+ \pi^-$, $\epsilon_{nm}^{K_L^0 \pi^+ \pi^- \text{ vs. } K_S^0 \pi^+ \pi^-}$, is a 128×128 matrix where each value of the indices n and m corresponds to one of the 128 distinct bin-pairs.

The peaking-background yields integrated over the Dalitz plot have been estimated for each DT in Sec. IV. The majority of the peaking backgrounds are CP eigenstates, for example the decay $D \rightarrow K_S^0 \pi^0$ forms a peaking background to the tag $D \rightarrow K_L^0 \pi^0$. The simulated data cannot accurately describe the distribution of the peaking background over the

Dalitz plot since it does not account for quantum correlations. For the peaking backgrounds which are CP eigenstates the expected yields are distributed according to Eq. (7) with an appropriate normalization factor to take into account the expected yield integrated over the Dalitz plot. The values of c_i and s_i used to make the initial estimate of the expected peaking background yields are computed from the $D \rightarrow K_S^0 \pi^+ \pi^-$ amplitude model [42]. As the yields of peaking backgrounds are small compared to the signal yields the effects of migration or small variations in efficiency over the Dalitz plot are ignored. A similar estimate for the peaking background of $D \rightarrow K_S^0 \pi^+ \pi^-$ vs. $D \rightarrow K_S^0 \pi^+ \pi^-$ in the $D \rightarrow K_L^0 \pi^+ \pi^-$ vs. $D \rightarrow K_S^0 \pi^+ \pi^-$ DT can be estimated through Eq. (9). The peaking background $D \rightarrow K_S^0 \pi^+ \pi^- \pi^0$ in the $D \rightarrow K_S^0 \omega$ tag is treated as CP -odd, as indicated by the results in Ref. [44]. The strong-phase parameters of $D \rightarrow \pi^+ \pi^- \pi^0 \pi^0$ are not known and in this case the peaking background is distributed as observed in simulated data. The expected distribution of the remaining peaking backgrounds that occur at low rates, such as $D \rightarrow \pi^+ \pi^- \pi^+ \pi^-$, are also taken from simulation.

D. Fit to determine c_i , c'_i , s_i and s'_i

To determine the values of $c_i^{(l)}$ and $s_i^{(l)}$, a log-likelihood fit is performed where the likelihood is given by

$$\begin{aligned}
-2\log\mathcal{L} = & -2\sum_{i=1}^8 \ln P(N_i^{\text{obs}}, \langle N_i^{\text{exp}} \rangle)_{CP, K_S^0 \pi^+ \pi^-} \\
& -2\sum_{i=1}^8 \ln P(N_i^{\text{obs}}, \langle N_i^{\text{exp}} \rangle)_{CP, K_L^0 \pi^+ \pi^-} \\
& -2\sum_{n=1}^{72} \ln P(N_n^{\text{obs}}, \langle N_n^{\text{exp}} \rangle)_{K_S^0 \pi^+ \pi^-, K_S^0 \pi^+ \pi^-} \\
& -2\sum_{n=1}^{128} \ln P(N_n^{\text{obs}}, \langle N_n^{\text{exp}} \rangle)_{K_L^0 \pi^+ \pi^-, K_S^0 \pi^+ \pi^-} \\
& + \chi^2, \tag{24}
\end{aligned}$$

where $P(N^{\text{obs}}, \langle N^{\text{exp}} \rangle)$ is the Poisson probability to observe N^{obs} events given the expected number $\langle N^{\text{exp}} \rangle$. The observed yield of signal and peaking background in the i th bin or n th bin-pair is denoted $N_{i,n}^{\text{obs}}$, and $N_{i,n}^{\text{exp}}$ is defined to account for both expected signal and peaking background from the same region. Biases can occur in the case where $N_{i,n}^{\text{obs}}$ is close to zero. To mitigate this effect the observed and expected yields of the three selections of $D \rightarrow K_S^0 \pi^+ \pi^-$ vs. $D \rightarrow K_S^0 \pi^+ \pi^-$ DT candidates are summed together. The observed and expected yields of the two final states of the $D \rightarrow K_S^0 \eta$ tag are also added together and the same is done for both final states of the $D \rightarrow K_S^0 \eta'$ tag. The χ^2 term in Eq. (24) is

$$\chi^2 = \sum_i \left(\frac{c'_i - c_i - \Delta c_i}{\delta \Delta c_i} \right)^2 + \sum_i \left(\frac{s'_i - s_i - \Delta s_i}{\delta \Delta s_i} \right)^2, \tag{25}$$

which constrains the measured differences $c'_i - c_i$ ($s'_i - s_i$) to the predicted differences, Δc_i (Δs_i), where $\delta \Delta c_i$ ($\delta \Delta s_i$) are the uncertainties in the predictions. The presence of the constraint is necessary in order to improve the precision of s_i and s'_i , and introduces very weak model assumptions in the fit. The expected values of c_i and s_i are determined from the $D \rightarrow K_S^0 \pi^+ \pi^-$ amplitude model in Ref. [42]. The expected values of c'_i and s'_i are determined from the assumed $D \rightarrow K_L^0 \pi^+ \pi^-$ amplitude model described in Sec. VB, where the central values come from the mean of the strong-phase distributions generated using different values of r and δ . In order to determine $\delta \Delta c_i$ and $\delta \Delta s_i$, the values of Δc_i and Δs_i are also estimated using the models of $D \rightarrow K_S^0 \pi^+ \pi^-$ reported in Refs. [45, 46] with the same transformation to estimate the $D \rightarrow K_L^0 \pi^+ \pi^-$ decay model. In order to assign $\delta \Delta c_i$ and $\delta \Delta s_i$, the larger deviation of the central values of Δc_i and Δs_i using these two alternative models is taken as part of the uncertainty and added in quadrature to the uncertainty from the choice of r and δ . The CP -tagged data can also be used to fit only c_i and c'_i where the likelihood does not contain a constraint on the difference between these parameters. The measured differences from this fit are consistent with the predicted values of Δc_i , which gives further confidence in

the transformations used to define the $D \rightarrow K_L^0 \pi^+ \pi^-$ amplitude model. Table VI summarizes the expected c_i , s_i , Δc_i and Δs_i and uncertainties for the three binning schemes.

To resolve the ambiguity in the sign of s_i present in Eqs. (22) and (23), the starting values of the parameters of the fit are set to be consistent with the model prediction. An iterative fit is performed to the data. After each iteration the expectation values of the peaking backgrounds that use c_i and s_i as input are recalculated using the c_i and s_i values determined by the fit. Three iterations are required to provide a stable result. The fitted strong-phase parameters c_i , s_i , c'_i , and s'_i are summarized in Table VII, in which both statistical and systematic uncertainties are included. Pseudo-experiments are used to validate the fit procedure. For each pseudo-experiment the simulated data yields in each bin are generated according a Poisson distribution based on the expectation using the values of $c_i^{(l)}$ and $s_i^{(l)}$ found in data. The resultant pull distributions for all strong-phase parameters are found to be consistent with normal distributions and hence the fit procedure is unbiased and returns Gaussian uncertainties.

Furthermore, several checks are performed to assess the stability of the fit results. The fits are repeated on different subsets of the data, for example, separating partially and fully-reconstructed $K_S^0 \pi^+ \pi^-$ events. Further tests involve removing specific tags, such as $\pi^+ \pi^- \pi^0$, $K_L^0 \pi^0$ and $K_L^0 \pi^0 \pi^0$. The results from these checks are consistent with the default values of $c_i^{(l)}$ and $s_i^{(l)}$. Furthermore, the c_i and s_i results are found to be robust when $K_L^0 \pi^+ \pi^-$ tags are removed from the fit.

VI. SYSTEMATIC UNCERTAINTIES

Uncertainties associated with the selection, tracking and PID efficiencies do not bias the measurement as the expected DT yields are calculated using the ST yields and determined values of $K_i^{(l)}$. This use of data-driven quantities to provide the normalization means that detector effects on the common selection affect the observed and expected DT yields in the same way, and hence these systematic uncertainties are not considered further.

Uncertainties on the ST yields, the $K_i^{(l)}$ parameters, and the efficiency matrices have an impact on the expected yields. Systematic uncertainties on the ST yields are determined by alternative fits to the M_{BC} distribution, in which the endpoint of the ARGUS function and the number of bins in the M_{BC} distribution are varied. An alternative data-driven method is used to determine the dominant peaking backgrounds. For example, the rate of the background from $D \rightarrow K_S^0 \pi^+ \pi^- \pi^0$ decays in $D \rightarrow K_S^0 \omega$ candidates is determined by analyzing the M_{BC} distribution of candidates whose $\pi^+ \pi^- \pi^0$ invariant mass falls in the side band of the reconstructed ω candidate mass distribution. The difference between this estimate and the nominal one from simulation is assigned as a systematic uncertainty. The total uncertainty on the measured ST yields comes from these sources added in quadrature to the statistical uncertainty from the fit. For the calculated yields, the uncertainty comes from the propagated uncertainties on $N_{D\bar{D}}$, the BFs, and efficiencies. The impact of the uncertainties on the

TABLE VI. The predicted values of c_i , s_i , Δc_i and Δs_i for three binning schemes using the model reported in Ref. [42].

bin	Equal $\Delta\delta_D$ binning				Optimal binning				Modified optimal binning			
	c_i	s_i	Δc_i	Δs_i	c_i	s_i	Δc_i	Δs_i	c_i	s_i	Δc_i	Δs_i
1	0.662	0.003	0.11 ± 0.03	0.01 ± 0.04	-0.018	-0.811	0.34 ± 0.10	0.08 ± 0.07	-0.356	-0.282	0.16 ± 0.12	-0.05 ± 0.10
2	0.622	0.423	0.17 ± 0.02	-0.06 ± 0.07	0.844	-0.133	0.12 ± 0.05	0.09 ± 0.12	0.805	-0.005	0.12 ± 0.01	0.01 ± 0.04
3	0.094	0.828	0.28 ± 0.08	-0.05 ± 0.06	0.187	-0.865	0.63 ± 0.04	0.38 ± 0.20	0.068	-0.727	0.50 ± 0.07	0.17 ± 0.14
4	-0.505	0.751	0.12 ± 0.09	0.06 ± 0.05	-0.913	-0.080	0.03 ± 0.04	-0.02 ± 0.06	-0.943	-0.112	0.03 ± 0.02	-0.03 ± 0.04
5	-0.948	-0.035	0.02 ± 0.02	-0.02 ± 0.05	-0.155	0.857	0.18 ± 0.12	0.01 ± 0.04	-0.354	0.807	0.13 ± 0.10	0.04 ± 0.04
6	-0.574	-0.562	0.24 ± 0.13	-0.06 ± 0.06	0.362	0.794	0.39 ± 0.16	-0.26 ± 0.11	0.257	0.782	0.34 ± 0.08	-0.13 ± 0.09
7	0.027	-0.794	0.49 ± 0.09	0.15 ± 0.12	0.864	0.206	0.04 ± 0.01	-0.03 ± 0.05	0.713	0.231	0.09 ± 0.03	-0.02 ± 0.06
8	0.442	-0.403	0.25 ± 0.04	0.11 ± 0.08	0.857	-0.333	0.01 ± 0.04	0.06 ± 0.13	0.784	-0.378	0.03 ± 0.04	0.08 ± 0.11

TABLE VII. The measured strong-phase difference parameters c_i , s_i , c'_i and s'_i , where the first uncertainties are statistical, including that related to the Δc_i and Δs_i constraints, and the second are systematic.

Equal $\Delta\delta_D$ binning				
	c_i	s_i	c'_i	s'_i
1	$0.708 \pm 0.020 \pm 0.009$	$0.128 \pm 0.076 \pm 0.017$	$0.801 \pm 0.020 \pm 0.013$	$0.137 \pm 0.078 \pm 0.017$
2	$0.671 \pm 0.035 \pm 0.016$	$0.341 \pm 0.134 \pm 0.015$	$0.848 \pm 0.036 \pm 0.016$	$0.279 \pm 0.137 \pm 0.016$
3	$0.001 \pm 0.047 \pm 0.019$	$0.893 \pm 0.112 \pm 0.020$	$0.174 \pm 0.047 \pm 0.016$	$0.840 \pm 0.118 \pm 0.021$
4	$-0.602 \pm 0.053 \pm 0.017$	$0.723 \pm 0.143 \pm 0.022$	$-0.504 \pm 0.055 \pm 0.019$	$0.784 \pm 0.147 \pm 0.022$
5	$-0.965 \pm 0.019 \pm 0.013$	$0.020 \pm 0.081 \pm 0.009$	$-0.972 \pm 0.021 \pm 0.017$	$-0.008 \pm 0.089 \pm 0.009$
6	$-0.554 \pm 0.062 \pm 0.024$	$-0.589 \pm 0.147 \pm 0.031$	$-0.387 \pm 0.069 \pm 0.025$	$-0.642 \pm 0.152 \pm 0.034$
7	$0.046 \pm 0.057 \pm 0.023$	$-0.686 \pm 0.143 \pm 0.028$	$0.462 \pm 0.056 \pm 0.019$	$-0.550 \pm 0.159 \pm 0.030$
8	$0.403 \pm 0.036 \pm 0.017$	$-0.474 \pm 0.091 \pm 0.027$	$0.640 \pm 0.036 \pm 0.015$	$-0.399 \pm 0.099 \pm 0.026$
Optimal binning				
	c_i	s_i	c'_i	s'_i
1	$-0.034 \pm 0.052 \pm 0.017$	$-0.899 \pm 0.094 \pm 0.030$	$0.240 \pm 0.054 \pm 0.014$	$-0.854 \pm 0.106 \pm 0.032$
2	$0.839 \pm 0.062 \pm 0.037$	$-0.272 \pm 0.166 \pm 0.031$	$0.927 \pm 0.054 \pm 0.036$	$-0.298 \pm 0.162 \pm 0.029$
3	$0.140 \pm 0.064 \pm 0.028$	$-0.674 \pm 0.172 \pm 0.038$	$0.742 \pm 0.060 \pm 0.030$	$-0.350 \pm 0.180 \pm 0.039$
4	$-0.904 \pm 0.021 \pm 0.009$	$-0.065 \pm 0.062 \pm 0.006$	$-0.930 \pm 0.023 \pm 0.019$	$-0.075 \pm 0.075 \pm 0.007$
5	$-0.300 \pm 0.042 \pm 0.013$	$1.047 \pm 0.055 \pm 0.019$	$-0.173 \pm 0.043 \pm 0.010$	$1.053 \pm 0.062 \pm 0.018$
6	$0.303 \pm 0.088 \pm 0.027$	$0.884 \pm 0.191 \pm 0.043$	$0.554 \pm 0.073 \pm 0.032$	$0.605 \pm 0.184 \pm 0.043$
7	$0.927 \pm 0.016 \pm 0.008$	$0.228 \pm 0.066 \pm 0.015$	$0.975 \pm 0.017 \pm 0.008$	$0.198 \pm 0.071 \pm 0.014$
8	$0.771 \pm 0.032 \pm 0.015$	$-0.316 \pm 0.123 \pm 0.021$	$0.798 \pm 0.035 \pm 0.017$	$-0.253 \pm 0.141 \pm 0.019$
Modified optimal binning				
	c_i	s_i	c'_i	s'_i
1	$-0.270 \pm 0.061 \pm 0.019$	$-0.140 \pm 0.168 \pm 0.028$	$-0.198 \pm 0.067 \pm 0.025$	$-0.209 \pm 0.181 \pm 0.028$
2	$0.829 \pm 0.027 \pm 0.018$	$-0.014 \pm 0.100 \pm 0.018$	$0.945 \pm 0.026 \pm 0.018$	$-0.019 \pm 0.100 \pm 0.017$
3	$0.038 \pm 0.044 \pm 0.021$	$-0.796 \pm 0.095 \pm 0.020$	$0.477 \pm 0.040 \pm 0.019$	$-0.709 \pm 0.119 \pm 0.028$
4	$-0.963 \pm 0.020 \pm 0.009$	$-0.202 \pm 0.080 \pm 0.014$	$-0.948 \pm 0.021 \pm 0.013$	$-0.235 \pm 0.086 \pm 0.014$
5	$-0.460 \pm 0.044 \pm 0.012$	$0.899 \pm 0.078 \pm 0.021$	$-0.359 \pm 0.046 \pm 0.011$	$0.943 \pm 0.084 \pm 0.022$
6	$0.130 \pm 0.055 \pm 0.017$	$0.832 \pm 0.131 \pm 0.031$	$0.333 \pm 0.051 \pm 0.019$	$0.701 \pm 0.137 \pm 0.029$
7	$0.762 \pm 0.025 \pm 0.012$	$0.178 \pm 0.094 \pm 0.016$	$0.878 \pm 0.026 \pm 0.015$	$0.188 \pm 0.098 \pm 0.016$
8	$0.699 \pm 0.035 \pm 0.012$	$-0.085 \pm 0.141 \pm 0.018$	$0.740 \pm 0.037 \pm 0.014$	$-0.025 \pm 0.149 \pm 0.019$

ST yields is investigated by performing multiple fits to data, where in each fit the ST yields used to calculate the expectation are varied according to their uncertainty. The resulting width of the distribution of the values of the strong-phase parameters is assigned as the systematic uncertainty associated with the ST yields.

The statistical uncertainties on the measured $K_i^{(\prime)}$ are propagated in a similar way, where the correlations between the measurements are taken into account. Systematic uncertainties also arise from the DCS correction factors, $f_i^{(\prime)}$, used to

determine the $K_i^{(\prime)}$ parameters. The uncertainties on $K_i^{(\prime)}$ are assigned by varying the input parameters in Table IV and by assessing the impact of using the alternative $D \rightarrow K_S^0 \pi^+ \pi^-$ models reported in Refs. [45] and [46] to calculate the $f_i^{(\prime)}$ factors. These systematic uncertainties on the $K_i^{(\prime)}$ are propagated to the strong-phase parameters. These different uncertainties on $K_i^{(\prime)}$ are combined in Tables VIII – X, where the statistical contribution is dominant.

A difference in the resolution between simulation and data introduces an uncertainty in the efficiency matrices. The dif-

ference in resolution is quantified by studying the mass spectrum of the $K^*(892)$ resonance found in $D \rightarrow K_S^0 \pi^+ \pi^-$ decays. The mass spectrum is fitted with a shape determined by simulation convolved with a Gaussian function, which defines the difference in resolution between data and simulation. The Gaussian has a mean of $0.23 \text{ MeV}/c^2$ and width $0.21 \text{ MeV}/c^2$. The variables $M_{K_S^0 \pi^-}$ and $M_{K_S^0 \pi^+}$ of all simulated events used to determine the efficiency matrices are smeared by a Gaussian with these parameters and new efficiency matrices are calculated. The same procedure is performed on the mass spectrum of $K^*(892)$ from $D \rightarrow K_L^0 \pi^+ \pi^-$ decays and the differences here are described with a Gaussian with mean $4.0 \text{ MeV}/c^2$ and width $2.0 \text{ MeV}/c^2$. The fit to determine the strong-phase parameters is repeated with the new efficiency matrices and the differences between these fit results and the nominal values are assigned as the systematic uncertainty due to residual differences between the momentum resolution in data and simulation. The impact of finite samples of simulated data to determine the efficiency matrices on the strong phases is assessed by varying the matrix elements by their statistical uncertainties. This is repeated multiple times, and the data are refitted using these new matrices to determine the expected yields. The resulting width of the distribution of the values of the strong-phase parameters is assigned as the systematic uncertainty due to the size of the simulated samples.

The expectation values of the peaking background have systematic uncertainties due to the inputs used to calculate their integrated yields and the assumptions concerning the distribution over the Dalitz plot. For the uncertainty from the integrated yields, the expected yield of peaking background in each phase space region is varied according to a Gaussian distribution. This distribution has the nominal value of the peaking-background yield as the mean, and a width which combines the uncertainties from the BFs of peaking-background decays, and the uncertainties arising from tracking [47], PID [47], and π^0 reconstruction efficiencies [48]. The distributions over the Dalitz plots for peaking backgrounds that are CP eigenstates, or $D \rightarrow K_S^0 \pi^+ \pi^-$ for $D \rightarrow K_L^0 \pi^+ \pi^-$ signals, are dependent on the values of c_i and s_i . As the iterative fit procedure recalculates the peaking background with updated values of c_i and s_i , no further systematic uncertainty is assigned for these backgrounds. The $D \rightarrow \pi^+ \pi^- \pi^0 \pi^0$ peaking background constitutes a significant contribution to the observed yields in $D \rightarrow K_S^0 \pi^+ \pi^-$ vs. $D \rightarrow K_S^0 \pi^+ \pi^-$ where one K_S^0 meson decays to the $\pi^0 \pi^0$ final state. To find an alternative distribution of this background a DT sample of $D \rightarrow K_S^0 \pi^+ \pi^-$ vs. $D \rightarrow \pi^+ \pi^- \pi^0 \pi^0$ events is fully reconstructed in data. The distribution over the Dalitz plot is found by assigning the K_S^0 mass to the π^0 pair. This distribution is used instead of the nominal one (from simulation) in the fit and small shifts are observed in the strong-phase parameters that are assigned as an additional contribution to the systematic uncertainties arising from the DT peaking backgrounds. Additionally, in Figs. 5(a) and 5(d), a few peaking backgrounds of the fitted combinatorial curves are not included in the nominal fit to extract the strong-phase parameters. To estimate their effects, a new fit is performed by including these peaking backgrounds and the difference between the

resulting fitted results and nominal values are taken as the other sources of systematic uncertainties.

The effects from $D^0 \bar{D}^0$ mixing are not considered in the nominal fit. The required correction factor for CP_{\pm} eigenstate ST yields is $1/(1 - \eta_{\pm} y_D)$, where $\eta_{\pm} = \pm 1$ and the mixing parameter $y_D = (0.62 \pm 0.08)\%$ [33]. The data are fitted using the corrected ST yields and the difference with respect to the nominal results is assigned as the systematic uncertainty due to charm mixing.

Systematic uncertainties in the observed DT yields arise from the fit procedure and the description of combinatorial background. Due to the low candidate yields in multiple of the phase space regions, small biases in the fitted yields can be present. The sizes of these biases are determined in pseudo-experiments. An alternative combinatorial background shape is employed and the difference in N^{obs} between this fit and the nominal is added in quadrature to the bias estimate to determine the systematic uncertainty on the observed yields. All the observed yields are smeared within these uncertainties and the fit is repeated. The resulting width of the distribution of values of the strong-phase parameters is assigned as the systematic uncertainty due to the DT yields.

The systematic uncertainties of the measured strong-phase parameters c_i , s_i , c'_i and s'_i for the equal $\Delta\delta_D$, optimal, and modified optimal binning schemes are summarized in Tables VIII, IX and X, respectively. There is no source of systematic uncertainty that is dominant for all strong-phase parameters. The statistical uncertainty obtained from the fit includes the contribution related to the associated uncertainties on Δc_i and Δs_i through the χ^2 term of Eq. (24). In order to estimate this contribution, the fit is repeated in a configuration where Δc_i and Δs_i are fixed. The difference in quadrature between the uncertainties from this fit and the nominal approach provides an estimate of the contribution to the uncertainty from the constraint. This estimate is also given in Tables VIII, IX and X, and it is seen that this contribution to the overall uncertainty is small. The measurements of the strong-phase parameters are limited by their statistical uncertainties. The correlation matrices for the statistical and systematic uncertainties associated with different binning schemes are given in Tables XI–XVI.

The measurements are displayed in Fig. 9, together with the model predictions from Ref. [42], which are seen to be in reasonable agreement. Given the compatibility between the current measurements and those reported by the CLEO collaboration [23] an additional set of fits is performed, where the CLEO results are imposed as a Gaussian constraint in Eq. (24). These results are presented in Appendix A.

VII. IMPACT ON γ/ϕ_3 MEASUREMENT

The model-independent measurement of γ described in Ref. [4] is performed by comparing the number of $B^- \rightarrow DK^-$, $D \rightarrow K_S^0 \pi^+ \pi^-$ events in a given Dalitz plot bin with the integral of the square of the amplitude given in Eq. (1) over the same region. An analogous expression for the B^+ events

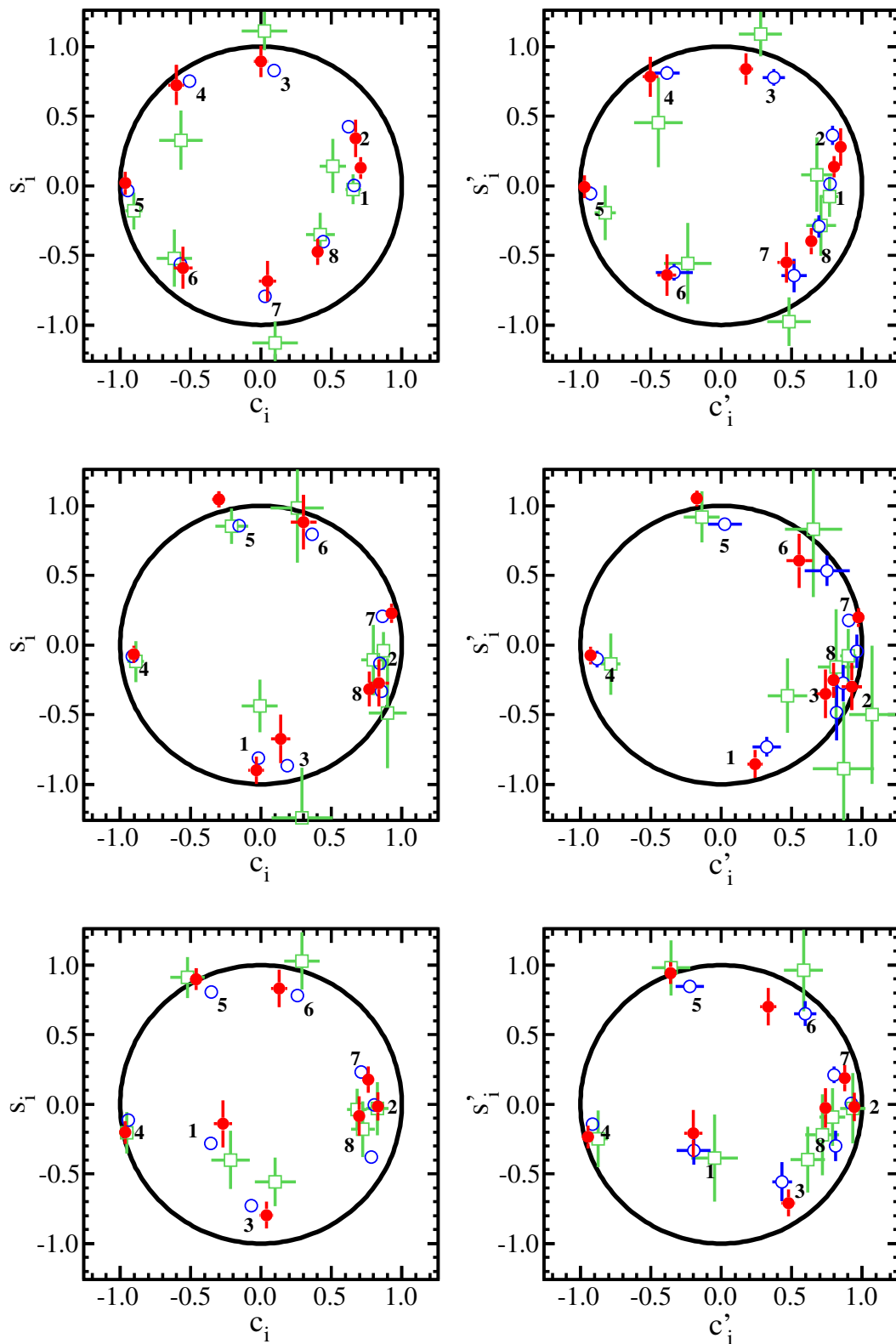


FIG. 9. The $c_i^{(j)}$ and $s_i^{(j)}$ measured in this work (red dots with error bars), the expected values from Ref. [42] (blue open circles) as well as CLEO results (green open squares with error bars) in Ref. [23]. The top plots are from the equal $\Delta\delta_D$ binning, the middle plots from the optimal binning and plots from the modified optimal binning scheme are on the bottom. The circle indicates the boundary of the physical region $c_i^{(j)2} + s_i^{(j)2} = 1$.

TABLE VIII. The uncertainties for c_i , s_i , c'_i and s'_i for the equal $\Delta\delta_D$ binning scheme.

Uncertainty	c_1	c_2	c_3	c_4	c_5	c_6	c_7	c_8
K_i and K'_i	0.004	0.013	0.005	0.007	0.005	0.014	0.006	0.007
ST yields	0.007	0.007	0.013	0.008	0.004	0.014	0.019	0.011
MC statistics	0.001	0.003	0.003	0.003	0.001	0.004	0.004	0.003
DT peaking-background subtraction	0.002	0.003	0.002	0.007	0.005	0.007	0.003	0.002
DT yields	0.001	0.002	0.002	0.001	0.001	0.002	0.003	0.002
Momentum resolution	0.002	0.003	0.012	0.011	0.010	0.010	0.011	0.009
$D^0\bar{D}^0$ mixing	0.001	0.000	0.002	0.001	0.000	0.002	0.002	0.001
Total systematic	0.009	0.016	0.019	0.017	0.013	0.024	0.023	0.017
Statistical plus $K_L^0\pi^+\pi^-$ model	0.020	0.035	0.047	0.053	0.019	0.062	0.057	0.036
$K_L^0\pi^+\pi^-$ model alone	0.011	0.009	0.027	0.030	0.007	0.034	0.033	0.017
Total	0.022	0.039	0.051	0.055	0.023	0.066	0.061	0.039

Uncertainty	s_1	s_2	s_3	s_4	s_5	s_6	s_7	s_8
K_i and K'_i	0.004	0.006	0.012	0.005	0.003	0.018	0.022	0.008
ST yields	0.001	0.001	0.001	0.001	0.001	0.002	0.001	0.001
MC statistics	0.007	0.011	0.009	0.010	0.005	0.009	0.011	0.006
DT peaking-background subtraction	0.007	0.005	0.007	0.018	0.005	0.009	0.011	0.004
DT yields	0.005	0.005	0.003	0.004	0.003	0.004	0.005	0.003
Momentum resolution	0.012	0.005	0.011	0.001	0.003	0.022	0.006	0.025
$D^0\bar{D}^0$ mixing	0.000	0.000	0.000	0.001	0.000	0.000	0.000	0.000
Total systematic	0.017	0.015	0.020	0.022	0.009	0.031	0.028	0.027
Statistical plus $K_L^0\pi^+\pi^-$ model	0.076	0.134	0.112	0.143	0.081	0.147	0.143	0.091
$K_L^0\pi^+\pi^-$ model alone	0.017	0.029	0.022	0.018	0.012	0.017	0.036	0.028
Total	0.078	0.135	0.114	0.144	0.081	0.150	0.146	0.095

Uncertainty	c'_1	c'_2	c'_3	c'_4	c'_5	c'_6	c'_7	c'_8
K_i and K'_i	0.006	0.014	0.009	0.006	0.005	0.012	0.014	0.009
ST yields	0.003	0.006	0.005	0.004	0.003	0.005	0.007	0.006
MC statistics	0.002	0.003	0.004	0.004	0.001	0.006	0.005	0.003
DT peaking-background subtraction	0.003	0.004	0.003	0.008	0.010	0.009	0.005	0.002
DT yields	0.002	0.002	0.003	0.002	0.001	0.004	0.004	0.003
Momentum resolution	0.010	0.003	0.009	0.015	0.012	0.017	0.001	0.009
$D^0\bar{D}^0$ mixing	0.002	0.001	0.004	0.002	0.000	0.005	0.006	0.003
Total systematic	0.013	0.016	0.016	0.019	0.017	0.025	0.019	0.015
Statistical plus $K_L^0\pi^+\pi^-$ model	0.020	0.036	0.047	0.055	0.021	0.069	0.056	0.036
$K_L^0\pi^+\pi^-$ model alone	0.012	0.010	0.028	0.033	0.011	0.046	0.032	0.017
Total	0.024	0.039	0.050	0.058	0.027	0.073	0.059	0.039

Uncertainty	s'_1	s'_2	s'_3	s'_4	s'_5	s'_6	s'_7	s'_8
K_i and K'_i	0.005	0.006	0.012	0.005	0.003	0.019	0.024	0.010
ST yields	0.002	0.001	0.001	0.001	0.000	0.002	0.001	0.001
MC statistics	0.007	0.011	0.009	0.010	0.005	0.009	0.013	0.007
DT peaking-background subtraction	0.007	0.004	0.008	0.019	0.005	0.010	0.009	0.004
DT yields	0.005	0.005	0.003	0.004	0.003	0.004	0.006	0.004
Momentum resolution	0.011	0.006	0.012	0.000	0.004	0.024	0.007	0.022
$D^0\bar{D}^0$ mixing	0.000	0.000	0.000	0.001	0.000	0.000	0.000	0.000
Total systematic	0.017	0.016	0.021	0.022	0.009	0.034	0.030	0.026
Statistical plus $K_L^0\pi^+\pi^-$ model	0.078	0.137	0.118	0.147	0.089	0.152	0.159	0.099
$K_L^0\pi^+\pi^-$ model alone	0.024	0.040	0.041	0.039	0.040	0.045	0.078	0.048
Total	0.080	0.137	0.119	0.147	0.090	0.156	0.162	0.103

is also used. Therefore the expected yield of B^\pm events in a Dalitz plot region is a function of K_i , c_i , s_i , and γ , δ_B and r_B , the underlying parameters of interest, and is given by

$$\begin{aligned}
N_{\pm i}^{\text{exp}}(B^- \rightarrow K^- D_{K_S^0 \pi^- \pi^+}) &= h_B^- \left[K_{\pm i} + r_B^2 K_{\mp i} + 2r_B \sqrt{K_i K_{-i}} \times [c_i \cos(\delta_B - \gamma) \pm s_i \sin(\delta_B - \gamma)] \right], \\
N_{\pm i}^{\text{exp}}(B^+ \rightarrow K^+ D_{K_S^0 \pi^- \pi^+}) &= h_B^+ \left[K_{\mp i} + r_B^2 K_{\pm i} + 2r_B \sqrt{K_i K_{-i}} \times [c_i \cos(\delta_B + \gamma) \mp s_i \sin(\delta_B + \gamma)] \right]. \quad (26)
\end{aligned}$$

In order to assess the impact of the uncertainty in the strong-phase parameters on a measurement of γ , a large simulated data set of B^\pm events is generated according to the expected distribution given the measured central values of K_i , c_i , and s_i and the input values $\gamma = 73.5^\circ$, $r_B = 0.103$, and $\delta_B = 136.9^\circ$, which are close to the current central values of these parameters from existing measurements [41]. The simulated data are fit many times to determine γ , δ_B and r_B . The values of c_i and s_i used in each fit are sampled from the measured values smeared by their uncertainties, where the correlations between the measurements are taken into account. The uncertainty on the measured K_i is not considered since experiments are expected to use their own data to provide this input [13]. The overall yield of the generated B^\pm sample is sufficiently large to ensure that the statistical uncertainty from the fit is negligible. Therefore the width of the distribution of the fitted value of γ is an estimate of the uncertainty on γ due to the precision of the strong-phase parameters. The distribution of the fitted value of γ in the three binning schemes is shown in Fig. 10.

Based on this study, the uncertainty on γ due to the measured uncertainty on c_i and s_i is found to be 0.7° , 1.2° and 0.8° for the equal $\Delta\delta_D$, optimal and modified optimal binning schemes, respectively. The very small phase space regions in the optimal binning scheme are the cause for the larger propagated uncertainty in this case. Very small biases of less than 0.2° are observed due to some values in the fit being unphysical, *i.e.* $c_i^2 + s_i^2 > 1$. The size of the uncertainty on γ is approximately a factor of three smaller than from the CLEO measurements [23]. The predicted statistical uncertainties on γ from LHCb prior to the start of High-Luminosity LHC operation in the mid 2020s, and from Belle II is expected to be 1.5° [49, 50]. Therefore the uncertainty associated to the strong-phase measurements presented here will not be dominant in the determination of γ for Belle II or for LHCb until then. The measurements of c_i and s_i can also be used for determination of strong-phase parameters in other multi-body decay modes of D mesons, where the $D^0 \rightarrow K_S^0 \pi^+ \pi^-$ decay is used as a tag [26, 37, 39, 44, 51]. Here, the improved precision leads to smaller systematic uncertainties on the strong-phase parameters in other D decay modes, which subsequently reduces associated systematic uncertainties on γ when these D decay modes are used to measure γ in $B^\pm \rightarrow DK^\pm$ decays.

VIII. SUMMARY

Measurements of the relative strong-phase differences between D^0 and $\bar{D}^0 \rightarrow K_{S,L}^0 \pi^+ \pi^-$ in bins of phase space have been performed using 2.93 fb^{-1} of data collected at $\sqrt{s}=3.773 \text{ GeV}$ collected with the BESIII detector. These results are on average a factor of 2.5 (1.9) more precise for c_i (s_i) and a

factor of 2.8 (2.2) more precise for c'_i (s'_i) than the previous measurements of these parameters [23]. This improvement arises from the combination of a larger data sample, an increased variety of CP tags, and broader use of the partial reconstruction technique to improve efficiency. The strong-phase parameters provide an important input in a wide range of CP violation measurements in the beauty and charm sectors. The propagated uncertainty from these measurements on the CKM parameter γ determined through the analysis of $B^\pm \rightarrow D_{K_S^0 \pi^+ \pi^-} K^\pm$ events is expected to be 0.7° , 1.2° and 0.8° for the equal $\Delta\delta_D$, optimal and modified optimal binning schemes, respectively. This improved precision will ensure that measurements of γ from LHCb and Belle II over the next decade are not limited by the knowledge of these strong-phase parameters, and also be invaluable in studies of charm mixing and CP violation.

IX. ACKNOWLEDGEMENTS

The BESIII collaboration thanks the staff of BEPCII and the IHEP computing center for their strong support. This work is supported in part by National Key Basic Research Program of China under Contract No. 2015CB856700; National Natural Science Foundation of China (NSFC) under Contracts Nos. 11625523, 11635010, 11735014, 11775027, 11822506, 11835012; the Chinese Academy of Sciences (CAS) Large-Scale Scientific Facility Program; Joint Large-Scale Scientific Facility Funds of the NSFC and CAS under Contracts Nos. U1532257, U1532258, U1732263, U1832207; CAS Key Research Program of Frontier Sciences under Contracts Nos. QYZDJ-SSW-SLH003, QYZDJ-SSW-SLH040; 100 Talents Program of CAS; INPAC and Shanghai Key Laboratory for Particle Physics and Cosmology; ERC under Contract No. 758462; German Research Foundation DFG under Contracts Nos. Collaborative Research Center CRC 1044, FOR 2359; Istituto Nazionale di Fisica Nucleare, Italy; Koninklijke Nederlandse Akademie van Wetenschappen (KNAW) under Contract No. 530-4CDP03; Ministry of Development of Turkey under Contract No. DPT2006K-120470; National Science and Technology fund; STFC (United Kingdom); The Knut and Alice Wallenberg Foundation (Sweden) under Contract No. 2016.0157; The Royal Society, UK under Contracts Nos. DH140054, DH160214; The Swedish Research Council; U. S. Department of Energy under Contracts Nos. DE-FG02-05ER41374, DE-SC-0010118, DE-SC-0012069; University of Groningen (RuG) and the Helmholtzzentrum fuer Schwerionenforschung GmbH (GSI), Darmstadt; This paper is also supported by Beijing municipal government under Contract No CIT&TCD201704047, and by the Royal Society under Contracts No. NF170002.

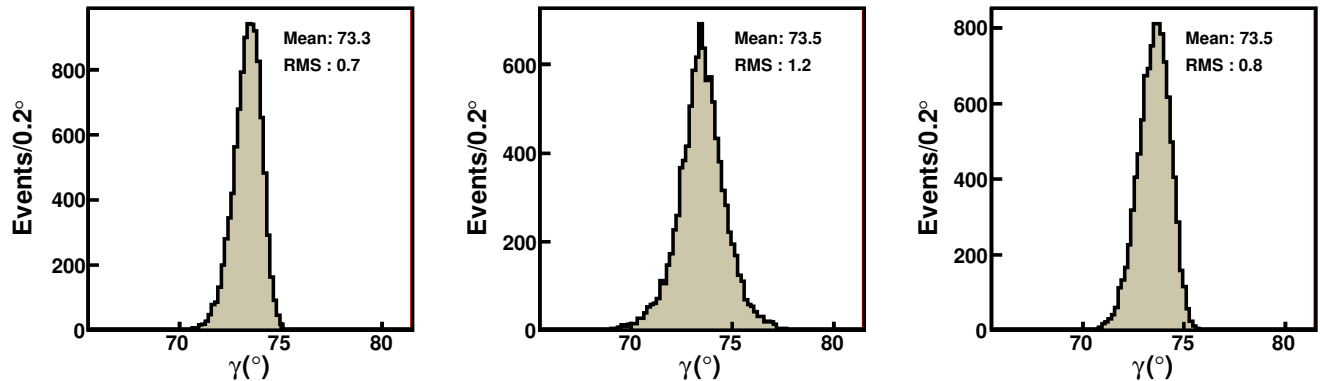


FIG. 10. The distribution of the fitted value of γ in the (left) equal $\Delta\delta_D$, (middle) optimal and (right) modified optimal binning schemes, respectively.

- [1] N. Cabibbo, Phys. Rev. Lett. **10**, 531 (1963); M. Kobayashi and T. Maskawa, Prog. Theor. Phys. **49**, 652 (1973).
- [2] J. Brod and J. Zupan, J. High Energy Phys. **01** (2014) 051.
- [3] M. Blanke and A. Buras, Eur. Phys. J. C **79**, 159 (2019).
- [4] A. Giri, Y. Grossman, A. Soffer, and J. Zupan, Phys. Rev. D **68**, 054018 (2003).
- [5] Y. Grossman, A. Soffer, and J. Zupan, Phys. Rev. D **72**, 031501(R) (2005).
- [6] A. Bondar, A. Poluektov and V. Vorobiev, Phys. Rev. D **82**, 034033 (2010).
- [7] A. Bondar and A. Poluektov, Eur. Phys. J. C **47**, 347 (2006); Eur. Phys. J. C **55**, 51 (2008).
- [8] A. Bondar, A. Dolgov, A. Poluektov and V. Vorobiev, Eur. Phys. J. C **73**, 2476 (2013).
- [9] M. Battaglieri *et al.*, Acta Phys. Polon. B **46**, 257 (2015).
- [10] R. Aaij *et al.* (LHCb Collaboration), Phys. Lett. B **718**, 43 (2012).
- [11] R. Aaij *et al.* (LHCb Collaboration), J. High Energy Phys. **10** (2014) 097.
- [12] R. Aaij *et al.* (LHCb Collaboration), J. High Energy Phys. **06** (2016) 131.
- [13] R. Aaij *et al.* (LHCb Collaboration), J. High Energy Phys. **08** (2018) 176; Erratum: J. High Energy Phys. **08** (2018) 107.
- [14] H. Aihara *et al.* (Belle Collaboration), Phys. Rev. D **85**, 112014 (2012).
- [15] T. Gershon and A. Poluektov, Phys. Rev. D **81**, 014025 (2010).
- [16] V. Vorobyev *et al.* (Belle Collaboration), Phys. Rev. D **94**, 052004 (2016).
- [17] A. Bondar, A. Kuzmina and V. Vorobyev, J. High Energy Phys. **03** (2018) 195.
- [18] C. Thomas and G. Wilkinson, J. High Energy Phys. **10** (2012) 185.
- [19] R. Aaij *et al.* (LHCb Collaboration), J. High Energy Phys. **04** (2016) 033.
- [20] A. D. Canto *et al.*, Phys. Rev. D **99**, 012007 (2019).
- [21] R. Aaij *et al.* (LHCb Collaboration), Phys. Rev. Lett. **122**, 231802 (2019).
- [22] R. A. Briere *et al.* (CLEO Collaboration), Phys. Rev. D **80**, 032002 (2009).
- [23] J. Libby *et al.* (CLEO Collaboration), Phys. Rev. D **82**, 112006 (2010).
- [24] M. Ablikim *et al.* (BESIII Collaboration), submitted to PRL, arXiv:2002.12791.
- [25] B. Aubert *et al.* (BaBar Collaboration), Phys. Rev. D **78**, 034023 (2008).
- [26] M. Nayak *et al.*, Phys. Lett. B **747**, 9 (2015).
- [27] M. Ablikim *et al.* (BESIII Collaboration), Nucl. Instrum. Methods Phys. Res., Sect. A **614**, 345 (2010).
- [28] S. Agostinelli *et al.* (GEANT4 Collaboration), Nucl. Instrum. Methods Phys. Res., Sect. A **506**, 250 (2003).
- [29] S. Jadach, B. F. L. Ward and Z. Was, Comput. Phys. Commun. **130**, 260 (2000); Phys. Rev. D **63**, 113009 (2001).
- [30] E. A. Kurav and V. S. Fadin, Sov. J. Nucl. Phys. **41**, 466 (1985) [Yad. Fiz. **41**, 733 (1985)].
- [31] E. Richter-Was, Phys. Lett. B **303**, 163 (1993).
- [32] D. J. Lange, Nucl. Instrum. Meth. A **462**, 152 (2001); R. G. Ping, Chin. Phys. C **32**, 599 (2008).
- [33] M. Tanabashi *et al.* (Particle Data Group), Phys. Rev. D **98**, 030001 (2018).
- [34] J. C. Chen, G. S. Huang, X. R. Qi, D. H. Zhang and Y. S. Zhu, Phys. Rev. D **62**, 034003 (2000).
- [35] H. Albrecht *et al.* (ARGUS Collaboration), Phys. Lett. B **241**, 278 (1990).
- [36] M. Ablikim, *et al.* (BESIII Collaboration), Chin. Phys. C **42**, 083001 (2018).
- [37] S. Harnew, P. Naik, C. Prouve, J. Rademacker and D. Asner, J. High Energy Phys. **01** (2018) 144.
- [38] D. Atwood and A. Soni, Phys. Rev. D **68**, 033003 (2003).
- [39] T. Evans, S.T. Harnew, J. Libby, S. Malde, J. Rademacker and G. Wilkinson, Phys. Lett. B **757**, 520 (2016).
- [40] T. Evans, S.T. Harnew, J. Libby, S. Malde, J. Rademacker and G. Wilkinson, Phys. Lett. B **765**, 402 (2017).
- [41] Y. Amhis *et al.*, (Heavy Flavor Averaging Group), Eur. Phys. J. C **77**, 895 (2017); and updates at <https://hflav.web.cern.ch>.
- [42] I. Adachi *et al.* (BaBar and Belle Collaborations), Phys. Rev. D **98**, 110212 (2018).
- [43] I. I. Bigi and H. Yamamoto, Phys. Lett. B **349**, 363 (1995).
- [44] P. K. Resmi, J. Libby, S. Malde and G. Wilkinson, J. High Energy Phys. **01** (2018) 082.

TABLE IX. The uncertainties of c_i , s_i , c'_i and s'_i for the optimal binning scheme.

Uncertainty	c_1	c_2	c_3	c_4	c_5	c_6	c_7	c_8
K_i and K'_i	0.003	0.032	0.023	0.005	0.005	0.015	0.007	0.012
ST yields	0.016	0.013	0.013	0.005	0.011	0.021	0.003	0.006
MC statistics	0.003	0.005	0.005	0.001	0.003	0.006	0.001	0.002
DT peaking-background subtraction	0.003	0.008	0.003	0.004	0.004	0.003	0.002	0.007
DT yields	0.002	0.004	0.004	0.001	0.002	0.003	0.001	0.001
Momentum resolution	0.004	0.007	0.002	0.005	0.001	0.001	0.002	0.001
$D^0\bar{D}^0$ mixing	0.003	0.002	0.003	0.001	0.003	0.005	0.000	0.000
Total systematic	0.017	0.037	0.028	0.009	0.013	0.027	0.008	0.015
Statistical plus $K_L^0\pi^+\pi^-$ model	0.052	0.062	0.064	0.021	0.042	0.088	0.016	0.032
$K_L^0\pi^+\pi^-$ model alone	0.031	0.034	0.025	0.012	0.027	0.062	0.003	0.013
Total	0.055	0.073	0.070	0.023	0.044	0.092	0.018	0.035

Uncertainty	s_1	s_2	s_3	s_4	s_5	s_6	s_7	s_8
K_i and K'_i	0.018	0.026	0.033	0.002	0.006	0.028	0.004	0.005
ST yields	0.001	0.001	0.001	0.001	0.001	0.002	0.001	0.001
MC statistics	0.006	0.013	0.012	0.003	0.003	0.017	0.004	0.011
DT peaking-background subtraction	0.012	0.009	0.011	0.004	0.015	0.013	0.011	0.015
DT yields	0.003	0.006	0.005	0.002	0.001	0.005	0.003	0.004
Momentum resolution	0.021	0.001	0.008	0.000	0.009	0.024	0.008	0.005
$D^0\bar{D}^0$ mixing	0.000	0.000	0.000	0.000	0.001	0.000	0.000	0.000
Total systematic	0.030	0.031	0.038	0.006	0.019	0.043	0.015	0.021
Statistical plus $K_L^0\pi^+\pi^-$ model	0.094	0.166	0.172	0.062	0.055	0.191	0.066	0.123
$K_L^0\pi^+\pi^-$ model alone	0.018	0.064	0.081	0.013	0.010	0.069	0.018	0.033
Total	0.099	0.169	0.176	0.062	0.058	0.196	0.068	0.125

Uncertainty	c'_1	c'_2	c'_3	c'_4	c'_5	c'_6	c'_7	c'_8
K_i and K'_i	0.009	0.032	0.027	0.005	0.006	0.028	0.007	0.015
ST yields	0.005	0.008	0.010	0.002	0.004	0.006	0.002	0.004
MC statistics	0.005	0.005	0.005	0.001	0.004	0.007	0.001	0.003
DT peaking-background subtraction	0.003	0.005	0.004	0.014	0.005	0.008	0.002	0.005
DT yields	0.003	0.004	0.005	0.001	0.002	0.004	0.001	0.002
Momentum resolution	0.004	0.008	0.002	0.011	0.001	0.005	0.003	0.001
$D^0\bar{D}^0$ mixing	0.006	0.005	0.004	0.001	0.004	0.006	0.001	0.002
Total systematic	0.014	0.036	0.030	0.019	0.010	0.032	0.008	0.017
Statistical plus $K_L^0\pi^+\pi^-$ model	0.054	0.054	0.060	0.023	0.043	0.073	0.017	0.035
$K_L^0\pi^+\pi^-$ model alone	0.033	0.013	0.013	0.014	0.029	0.038	0.006	0.020
Total	0.056	0.065	0.068	0.030	0.045	0.080	0.019	0.039

Uncertainty	s'_1	s'_2	s'_3	s'_4	s'_5	s'_6	s'_7	s'_8
K_i and K'_i	0.019	0.023	0.031	0.003	0.006	0.025	0.004	0.008
ST yields	0.001	0.001	0.001	0.001	0.001	0.002	0.001	0.001
MC statistics	0.007	0.015	0.016	0.004	0.003	0.016	0.005	0.013
DT peaking-background subtraction	0.013	0.007	0.005	0.004	0.012	0.012	0.010	0.009
DT yields	0.003	0.006	0.005	0.002	0.001	0.005	0.003	0.005
Momentum resolution	0.021	0.004	0.014	0.002	0.012	0.027	0.008	0.006
$D^0\bar{D}^0$ mixing	0.000	0.000	0.000	0.000	0.000	0.000	0.000	0.000
Total systematic	0.032	0.029	0.039	0.007	0.018	0.043	0.014	0.019
Statistical plus $K_L^0\pi^+\pi^-$ model	0.106	0.162	0.180	0.075	0.062	0.184	0.071	0.141
$K_L^0\pi^+\pi^-$ model alone	0.051	0.054	0.097	0.045	0.030	0.044	0.031	0.076
Total	0.111	0.165	0.184	0.076	0.064	0.189	0.073	0.143

[45] A. Poluektov *et al.* (Belle Collaboration), Phys. Rev. D **81**, 112002 (2010).[46] B. Aubert *et al.* (BaBar Collaboration), Phys. Rev. Lett. **95**, 121802 (2005).[47] M. Ablikim *et al.* (BESIII Collaboration), Phys. Rev. D **99**, 011103 (2019).[48] M. Ablikim *et al.* (BESIII Collaboration), Phys. Rev. Lett. **123**, 112001 (2019).

TABLE X. The uncertainties of c_i , s_i , c'_i and s'_i for the modified optimal binning scheme.

Uncertainty	c_1	c_2	c_3	c_4	c_5	c_6	c_7	c_8
K_i and K'_i	0.007	0.014	0.005	0.005	0.005	0.008	0.006	0.009
ST yields	0.013	0.006	0.018	0.004	0.008	0.014	0.005	0.007
MC statistics	0.004	0.002	0.003	0.001	0.003	0.004	0.002	0.002
DT peaking-background subtraction	0.005	0.004	0.005	0.004	0.006	0.002	0.002	0.003
DT yields	0.002	0.002	0.003	0.001	0.001	0.002	0.001	0.001
Momentum resolution	0.010	0.008	0.007	0.006	0.000	0.005	0.008	0.000
$D^0\bar{D}^0$ mixing	0.002	0.001	0.002	0.000	0.002	0.002	0.000	0.000
Total systematic	0.019	0.018	0.021	0.009	0.012	0.017	0.012	0.012
Statistical plus $K_L^0\pi^+\pi^-$ model	0.061	0.027	0.044	0.020	0.044	0.055	0.025	0.035
$K_L^0\pi^+\pi^-$ model alone	0.034	0.006	0.028	0.008	0.027	0.033	0.011	0.015
Total	0.064	0.032	0.048	0.022	0.046	0.058	0.027	0.037

Uncertainty	s_1	s_2	s_3	s_4	s_5	s_6	s_7	s_8
K_i and K'_i	0.010	0.011	0.014	0.004	0.005	0.013	0.005	0.008
ST yields	0.001	0.002	0.001	0.001	0.002	0.002	0.001	0.001
MC statistics	0.011	0.009	0.007	0.005	0.005	0.011	0.008	0.013
DT peaking-background subtraction	0.023	0.009	0.005	0.013	0.019	0.021	0.008	0.007
DT yields	0.006	0.005	0.004	0.003	0.002	0.004	0.005	0.006
Momentum resolution	0.000	0.002	0.011	0.000	0.001	0.015	0.010	0.002
$D^0\bar{D}^0$ mixing	0.000	0.001	0.000	0.000	0.001	0.000	0.000	0.000
Total systematic	0.028	0.018	0.020	0.014	0.021	0.031	0.016	0.018
Statistical plus $K_L^0\pi^+\pi^-$ model	0.168	0.100	0.095	0.080	0.078	0.131	0.094	0.141
$K_L^0\pi^+\pi^-$ model alone	0.029	0.021	0.037	0.010	0.013	0.035	0.026	0.041
Total	0.170	0.102	0.097	0.081	0.081	0.134	0.096	0.143

Uncertainty	c'_1	c'_2	c'_3	c'_4	c'_5	c'_6	c'_7	c'_8
K_i and K'_i	0.008	0.014	0.012	0.005	0.004	0.014	0.007	0.012
ST yields	0.005	0.005	0.007	0.003	0.003	0.006	0.003	0.004
MC statistics	0.005	0.002	0.004	0.001	0.004	0.005	0.002	0.003
DT peaking-background subtraction	0.005	0.003	0.004	0.009	0.003	0.005	0.003	0.003
DT yields	0.004	0.002	0.004	0.001	0.002	0.003	0.002	0.002
Momentum resolution	0.021	0.008	0.011	0.008	0.007	0.007	0.013	0.000
$D^0\bar{D}^0$ mixing	0.004	0.002	0.006	0.001	0.003	0.004	0.002	0.002
Total systematic	0.025	0.018	0.019	0.013	0.011	0.019	0.015	0.014
Statistical plus $K_L^0\pi^+\pi^-$ model	0.067	0.026	0.040	0.021	0.046	0.051	0.026	0.037
$K_L^0\pi^+\pi^-$ model alone	0.043	0.004	0.021	0.010	0.031	0.027	0.014	0.019
Total	0.071	0.032	0.044	0.025	0.048	0.055	0.030	0.039

Uncertainty	s'_1	s'_2	s'_3	s'_4	s'_5	s'_6	s'_7	s'_8
K_i and K'_i	0.011	0.011	0.020	0.005	0.005	0.012	0.006	0.009
ST yields	0.002	0.002	0.001	0.001	0.002	0.002	0.001	0.001
MC statistics	0.011	0.009	0.010	0.005	0.005	0.011	0.008	0.013
DT peaking-background subtraction	0.022	0.008	0.005	0.012	0.020	0.016	0.008	0.008
DT yields	0.007	0.005	0.005	0.003	0.002	0.004	0.005	0.007
Momentum resolution	0.002	0.002	0.015	0.000	0.002	0.018	0.009	0.001
$D^0\bar{D}^0$ mixing	0.000	0.001	0.000	0.000	0.001	0.000	0.000	0.000
Total systematic	0.028	0.017	0.028	0.014	0.022	0.029	0.016	0.019
Statistical plus $K_L^0\pi^+\pi^-$ model	0.181	0.100	0.119	0.086	0.084	0.137	0.098	0.149
$K_L^0\pi^+\pi^-$ model alone	0.073	0.022	0.081	0.033	0.034	0.054	0.037	0.061
Total	0.183	0.102	0.122	0.087	0.087	0.140	0.099	0.150

- [49] I. Bediaga *et al.* (LHCb Collaboration), HCB-PUB-2018-009, CERN-LHCC-2018-027 [arXiv:1808.08865].
- [50] E. Kou *et al.* (Belle II Collaboration), KEK Preprint 2018-27, BELLE2-PUB-PH-2018-001, FERMILAB-PUB-18-398-T, JLAB-THY-18-2780, INT-PUB-18-047, UWThPh 2018-26

- [arXiv:1808.10567].
- [51] J. Insler *et al.* (CLEO Collaboration), Phys. Rev. D **85**, 092016 (2012).

X. APPENDIX A

As the results presented here and those from the CLEO collaboration [23] are compatible it is legitimate to combine them in order to provide a single set of results that benefits from both measurements. The combination is performed by performing the fit described in Sec. V to the double tags with an additional multi-dimensional Gaussian constraint present on the strong-phase parameters. This constraint comes from the central values and the covariance matrices in Ref. [23].

A small, additional contribution to these covariance matrices, determined through pseudo-experiments, accounts for the effects reported in Ref. [40].

The systematic uncertainties reported in Tables VIII – X are added in quadrature to those from the fit, which include contributions from the BESIII statistical and CLEO statistical and systematic uncertainties. The central values and their uncertainties for the three binning schemes are reported in Table XVII and Tables XVIII, XIX, and XX show the associated covariance matrices.

TABLE XVII. The measured strong-phase difference parameters c_i , s_i , c'_i and s'_i where the results reported in Ref. [23] are used as a constraint.

Equal binning scheme				
	c_i	s_i	c'_i	s'_i
1	0.699 ± 0.020	0.091 ± 0.063	0.800 ± 0.023	0.101 ± 0.065
2	0.643 ± 0.036	0.300 ± 0.110	0.823 ± 0.037	0.266 ± 0.116
3	0.001 ± 0.047	1.000 ± 0.075	0.186 ± 0.047	0.946 ± 0.083
4	-0.608 ± 0.052	0.660 ± 0.123	-0.512 ± 0.055	0.730 ± 0.129
5	-0.955 ± 0.023	-0.032 ± 0.069	-0.961 ± 0.027	-0.060 ± 0.079
6	-0.578 ± 0.058	-0.545 ± 0.122	-0.371 ± 0.069	-0.610 ± 0.131
7	0.057 ± 0.057	-0.854 ± 0.095	0.464 ± 0.055	-0.715 ± 0.105
8	0.411 ± 0.036	-0.433 ± 0.083	0.656 ± 0.036	-0.350 ± 0.092
Optimal binning scheme				
	c_i	s_i	c'_i	s'_i
1	-0.037 ± 0.049	-0.829 ± 0.097	0.265 ± 0.052	-0.791 ± 0.109
2	0.837 ± 0.067	-0.286 ± 0.152	0.939 ± 0.062	-0.290 ± 0.155
3	0.147 ± 0.067	-0.786 ± 0.154	0.744 ± 0.064	-0.427 ± 0.170
4	-0.905 ± 0.021	-0.079 ± 0.059	-0.916 ± 0.029	-0.090 ± 0.073
5	-0.291 ± 0.041	1.022 ± 0.064	-0.176 ± 0.042	1.041 ± 0.069
6	0.272 ± 0.082	0.977 ± 0.176	0.558 ± 0.074	0.693 ± 0.172
7	0.918 ± 0.017	0.184 ± 0.065	0.965 ± 0.018	0.160 ± 0.070
8	0.773 ± 0.033	-0.277 ± 0.118	0.800 ± 0.037	-0.236 ± 0.137
Modified optimal binning scheme				
	c_i	s_i	c'_i	s'_i
1	-0.268 ± 0.056	-0.239 ± 0.139	-0.161 ± 0.063	-0.285 ± 0.156
2	0.825 ± 0.031	-0.026 ± 0.092	0.941 ± 0.031	-0.030 ± 0.093
3	0.048 ± 0.045	-0.743 ± 0.088	0.491 ± 0.042	-0.638 ± 0.105
4	-0.961 ± 0.021	-0.208 ± 0.072	-0.943 ± 0.024	-0.241 ± 0.079
5	-0.472 ± 0.042	0.910 ± 0.068	-0.364 ± 0.045	0.959 ± 0.075
6	0.158 ± 0.052	0.881 ± 0.114	0.369 ± 0.051	0.753 ± 0.123
7	0.747 ± 0.026	0.124 ± 0.085	0.864 ± 0.029	0.132 ± 0.090
8	0.703 ± 0.034	-0.142 ± 0.119	0.741 ± 0.037	-0.092 ± 0.131

